

JGR Solid Earth

RESEARCH ARTICLE

10.1029/2024JB029836

Key Points:

- The hectometer-scale hydraulic stimulation experiments fill the gap between decameter experiments and the km scale of engineering projects
- Hydro-geomechanical response of a complex 100 m+ fracture networks imaged by pico-seismic events
- Seismicity occurs on preexisting fractures, activating dominantly the ones well-oriented within the stress field for hydro-shearing

Supporting Information:

Supporting Information may be found in the online version of this article.

Correspondence to:

A. Obermann,
anne.obermann@sed.ethz.ch

Citation:

Obermann, A., Rosskopf, M., Durand, V., Plenkers, K., Bröker, K., Rinaldi, A. P., et al. (2024). Seismic response of hectometer-scale fracture systems to hydraulic stimulation in the Bedretto underground laboratory, Switzerland. *Journal of Geophysical Research: Solid Earth*, 129, e2024JB029836. <https://doi.org/10.1029/2024JB029836>

Received 3 JUL 2024

Accepted 17 OCT 2024

Author Contributions:

Conceptualization: Anne Obermann, Katrin Plenkers, Marian Hertrich, Xiaodong Ma, Hansruedi Maurer, Domenico Giardini

Data curation: Anne Obermann, Martina Rosskopf, Kai Bröker, Nima Gholizadeh Doonechaly, Marian Hertrich, Xiaodong Ma

Formal analysis: Anne Obermann, Martina Rosskopf, Virginie Durand, Kai Bröker, Antonio Pio Rinaldi, Nima Gholizadeh Doonechaly

Funding acquisition: Stefan Wiemer, Domenico Giardini

© 2024. The Author(s).

This is an open access article under the terms of the Creative Commons Attribution-NonCommercial-NoDerivs License, which permits use and distribution in any medium, provided the original work is properly cited, the use is non-commercial and no modifications or adaptations are made.

Seismic Response of Hectometer-Scale Fracture Systems to Hydraulic Stimulation in the Bedretto Underground Laboratory, Switzerland

Anne Obermann^{1,2} , Martina Rosskopf^{1,2} , Virginie Durand² , Katrin Plenkers³ , Kai Bröker^{2,4} , Antonio Pio Rinaldi¹ , Nima Gholizadeh Doonechaly^{2,4} , Valentin Gischig^{1,5} , Alba Zappone¹ , Florian Amann⁶ , Massimo Cocco⁷ , Marian Hertrich² , Mohammadreza Jalali⁶ , Jonas Simon Junker¹ , Philipp Kästli¹ , Xiaodong Ma² , Hansruedi Maurer² , Men-Andrin Meier², Miriam Schwarz^{1,2}, Paul Selvadurai¹, Linus Villiger^{1,2} , Stefan Wiemer¹ , Luca Dal Zilio^{2,8,9} , and Domenico Giardini²

¹Swiss Seismological Service, ETH Zurich, Zurich, Switzerland, ²Institute of Geophysics, ETH Zurich, Zurich, Switzerland, ³Gesellschaft für Materialprüfung und Geophysik mbH (GMuG), Bad Nauheim, Germany, ⁴Center for Hydrogeology and Geothermics, University of Neuchâtel, Neuchâtel, Switzerland, ⁵Institute of Geology, ETH Zurich, Zurich, Switzerland, ⁶Department of Engineering Geology and Hydrogeology, RWTH Aachen University, Aachen, Germany, ⁷Sezione Roma 1, Istituto Nazionale di Geofisica e Vulcanologia, Rome, Italy, ⁸Earth Observatory of Singapore, Nanyang Technological University, Singapore, Singapore, ⁹Asian School of the Environment, Nanyang Technological University, Singapore, Singapore

Abstract We performed a series of hydraulic stimulations at 1.1 km depth in the Bedretto underground laboratory, Switzerland, as part of an overall research strategy attempting to understand induced seismicity on different scales. Using an ultra-high frequency seismic network we detect seismic events as small as $M_w < -4$, revealing intricate details of a complex fracture network extending over 100 m from the injection sites. Here, we outline the experimental approach and present seismic catalogs as well as a comparative analysis of event number per injection, magnitudes, b -values, seismogenic index and reactivation pressures. In our first-order seismicity analysis, we could make the following observations: The rock volume impacted by the stimulations in different intervals differs significantly with a lateral extent from a few meters to more than 150 m. In most intervals multiple fractures were reactivated. The seismicity typically propagates upwards toward shallower depth on parallel oriented planes that are consistent with the stress field and seem to a large extent associated with preexisting open fractures. This experiment confirms the diversity in seismic behavior independent from the injection protocol. The overall seismicity patterns demonstrate that multi-stage stimulations using zonal isolation allow developing an extended fracture network in a 3D rock volume, which is necessary for enhanced geothermal systems. Our stimulations covering two orders of magnitude in terms of injected volume will give insights into upscaling of induced seismicity from underground laboratory scale to field scale.

Plain Language Summary The Bedretto Underground Laboratory offers ideal conditions for studies focusing on the behavior of the deep underground. In this unique research facility, we built a geothermal test reservoir consisting of a set of injection/production boreholes with up to 400 m length drilled from the tunnel. In 2022 and 2023, we performed various stimulation experiments in packed off sections of this hectometer rock volume. The stimulations were monitored by a newly developed densely spaced multiparameter seismic and hydro-mechanical monitoring system. The data show the activation of faults with linear dimensions approaching and passing 100 m, yielding a clear impression of a hectometer fractured reservoir.

1. Introduction

Exploitation of geothermal energy from deep fractured reservoirs is suggested as an important player in future energy productions across central Europe (Hirschberg et al., 2015). Developing such deep reservoirs (i.e., enhancing permeability and connectivity between boreholes) requires knowledge of the geometry of fracture networks and fluid flow paths, along with their reaction to injection and production (e.g., Barbier, 2002; Gholizadeh Doonechaly et al., 2023). Key challenges for geothermal power production are establishing sustainable flow rates at sufficient fluid temperatures and, to a varying extent, controlling induced seismicity (e.g., Edwards et al., 2015; Ellsworth et al., 2019; Kwiatek et al., 2019). Both topics are closely related to the fracture network of

Investigation: Anne Obermann,

Martina Rosskopf

Methodology: Anne Obermann**Resources:** Katrin Plenkers,

Marian Hertrich, Philipp Kästli

Software: Anne Obermann,

Martina Rosskopf, Virginie Durand

Supervision: Anne Obermann**Visualization:** Anne Obermann,

Martina Rosskopf, Virginie Durand,

Antonio Pio Rinaldi, Alba Zappone

Writing – original draft:

Anne Obermann, Martina Rosskopf,

Virginie Durand, Katrin Plenkers,

Kai Bröker, Antonio Pio Rinaldi,

Valentin Gischig, Alba Zappone

Writing – review & editing:

Anne Obermann, Martina Rosskopf,

Katrin Plenkers, Kai Bröker, Antonio

Pio Rinaldi, Nima Gholizadeh

Dooonechaly, Valentin Gischig,

Alba Zappone, Florian Amann,

Massimo Cocco, Mohammadreza Jalali,

Jonas Simon Junker, Philipp Kästli,

Men-Andrin Meier, Miriam Schwarz,

Paul Selvadurai, Linus Villiger, Luca Dal

Zilio, Domenico Giardini

the reservoir in connection with the in situ stress field. An accurate analysis of injection induced micro-seismicity (e.g., Diehl et al., 2017) and monitoring of accompanying aseismic processes (e.g., Adelinet et al., 2016; Hillers et al., 2015; Obermann et al., 2015; Sanchez-Pastor et al., 2019, 2023; Taira et al., 2018; Toledo et al., 2022) contribute to the detailed process understanding of the coupled seismo-hydro-mechanical processing during the exploration and operation phases. This understanding is essential to reduce the high project risk and upstream exploration costs that remain key barriers to scaling up of geothermal energy development, globally.

Extensive literature is dedicated to the hydro-seismo-mechanical processes taking place in single fractures (Goodman, 1989; Jaeger et al., 2007; Ye & Ghassemi, 2018, and references therein). The fundamental mechanisms have been understood as the interplay between stress, permeability and seismicity. However, it remains challenging to understand the stimulation induced hydro-seismo-mechanical processes in fractured rock masses (Amann et al., 2018, and references therein), specifically, the upscaling from the laboratory to the field scale. To close the gap between laboratory experiments and natural, full-scale observations, in situ injection experiments have become a backbone of geo-energy research (Amann et al., 2018; Boese et al., 2022; Gischig et al., 2020; Manthei et al., 2001; Zang et al., 2017). In situ experiments in underground laboratories allow us to monitor the rock volume with all its complexity in much greater detail than possible in full-scale operation at great depths. This provides us with the possibility to gain inherent process understanding given the better accessibility and controllability for experimental work. Moreover, in situ experiments offer the possibility to develop new technologies at lower costs and risks, (e.g., innovative borehole completion and hydraulic stimulation approaches) which can be transferred in the next step to full-scale operations.

A key challenge in reservoir operations is the limited knowledge of the fracture network, which can often only be illuminated with induced seismicity monitoring that benefits from the ability to detect and locate very weak events. The potential of very-broadband and ultra-high-frequency seismic networks to map out fracture networks and gain process understanding has successfully been demonstrated in mines (Plenkers et al., 2022). Naoi et al. (2011) outlined in this way the complex fault geometry (100 m × 80 m) and the interaction with the neighboring fracture network of an M2 event in the Mponeng Gold mine, South Africa. The same data set allowed, for example, to identify asperity weakening processes (Yabe et al., 2015), seismic energy partitioning (Kwiatek et al., 2011), and estimation of radiated energies (Kwiatek & Ben-Zion 2013; Naoi, Nakatani, Otsuki, et al., 2015) used a similar network to map pre-existing faults and newly developed shear zones in the context of a migrating mining front in a rock volume of approx. 200 m × 250 m × 100 m. The data could be used to understand quasi-static slip and aseismic creep within the fracture network by the analysis of repeating events, focal mechanisms and the temporal-spatial evolution. They could also provide insights into the probability of inducing a larger event by *b*-value analysis (Naoi, Nakatani, Igarashi, et al., 2015; Naoi, Nakatani, Kgarume, et al., 2015). Knowing that some of the existent shear zones are prone to violent failure (e.g., Gibowicz & Kijko, 1994; McGarr, 1971; Van Aswegen, 2005) and therefore a risk in the mining operation, helps significantly in planning the excavations. Ultra-high frequency networks were also successfully used in decameter-scale injection experiments, where the activation of decameter-scale fracture systems was successfully outlined (Boese et al., 2022; Jalali et al., 2018; Manthei et al., 2001; Villiger et al., 2020; Zang et al., 2017).

Here, we apply the techniques developed in mines and underground laboratories, where experiments take place in the rock volume that is accessible for people and sensor installations by galleries and stopes, to geoenergy research at the Bedretto Underground Laboratory for Geoenergy and Geoscience (BULGG). This new, deep underground experimental facility has been developed since 2018 in the Bedretto Tunnel in the Swiss Alps. The laboratory has an average overburden of 1 km, providing an advantageous accessibility to a rock mass that is comparable to shallow crystalline reservoirs in terms of stress conditions and structure. A geothermal test reservoir (Bedretto Geothermal Testbed) was built consisting of a set of injection/production boreholes with up to 400 m length drilled from the tunnel.

The ultimate goal of the facility is to develop novel technologies and operational procedures to increase efficiency and safety of geothermal exploration and production and thus, ultimately, supporting economic feasibility and societal acceptance. BULGG continues the strategy of bridging the investigation scale from laboratory centimeter-scale and decameter in situ scale to the full operational scale (km), as well as from a pure focus on process understanding to piloting strategies and technologies, which was initiated at the Grimsel Test Site (Amann et al., 2018; Gischig et al., 2020) and various places world-wide (STIMTEC, Boese et al., 2022; Aspö, Kwiatek et al., 2018; EGS Collab, Kneafsey et al., 2018; FORGE, Allis et al., 2016).

In the Bedretto Geothermal Testbed, we were able to characterize the host rock in large detail and systematically develop the reservoir in separate phases under controlled conditions. The hectometer long boreholes were characterized with georadar and wireline logging tools to reconstruct the fracture network along and beyond the borehole side wall at distances of a few centimeters to decameters. While the fracture network characterization using these techniques can easily be biased due to shadowing effects of strong reflectors, additional information may be gained from mapping of seismicity recorded with a dense sensor network that yields small location uncertainties, allowing observations at high resolution far into the rock volume.

In 2022 and 2023, we performed 13 stimulation experiments in 8 packed off sections of a hectometer rock volume as part of the Bedretto Reservoir Project (BRP). The BRP encompasses three sub-projects with complementary targets for the development of a large-scale deep reservoir for the circulation of water and the storage and extraction of geothermal energy; **VALTER** (Validating of technologies for reservoir engineering, Giardini et al., 2022), **DESTRESS** (Demonstration of soft stimulation treatments of geothermal reservoirs) and **ZoDrEx** (zonal Isolation, Drilling and Exploitation of EGS projects, Meier & Christe, 2023; Meier et al., 2020). The stimulations presented here were part of the VALTER project and monitored by a newly developed densely spaced multiparameter seismic and hydro-mechanical monitoring system (Plenkers et al., 2023). In particular, a seismic network was built inside the boreholes allowing sensitive measurements in the near and far field over a very wide range of frequencies (0.08 Hz–100 kHz). This project aims to understand the physical processes driving hydraulic stimulations, enhance hydraulic conductivity and permeability within a geothermal reservoir with minimal seismic activity, optimize injection strategies, and develop effective sensor layouts for future deep geothermal systems.

Our data show the activation of faults with linear dimensions approaching and passing 100 m, yielding a clear impression of a hectometer fractured reservoir, allowing us to address questions associated with the variability of the seismic response in relation with a distinct hydro-mechanical characterization, the upscaling capabilities, as well as the impact of different injection strategies.

2. Test Site and Experimental Setup

Since 2018, ETH has been developing the BedrettoLab, a new deep underground experimental facility in the Swiss Alps, near the Gotthard pass region (Figure 1a). This region shows a low level of background seismicity, which was considered advantageous in the sites' risk assessment (Gischig et al., 2019). The BedrettoLab is located in the 5.2 km long Bedretto Tunnel that connects the Furka Base Tunnel in the northwest with the Bedretto valley in the southeast (Figures 1a and 1b, modified after Ceccato et al. (2024)) and was originally used to facilitate ventilation and drainage of the Furka Base Tunnel. Since its completion in 1982, the Bedretto Tunnel remained largely unlined and unpaved, offering direct access to the rock volume, composed mainly by a granitic intrusion known in literature as Rotondo Granite (Fritsch, 1873; Rutsch & Pruvost, 1966). In 2018, the owner, the Matterhorn Gotthard Infrastructure (MGI), gave access to the tunnel to ETH Zürich for long-term research, which prompted the establishment of the BedrettoLab. The Bedretto Geothermal Testbed, where the here presented experiments took place, is operated from a 6 m by 3 m by 100 m (width, height, length) niche at 2 km from the southern tunnel entrance within the Rotondo Granite. The local overburden is 1,000 m (Figure 1b).

2.1. Geology and In-Situ Stress at the Bedretto Geothermal Testbed

The geology at the experiment location is dominated by the Rotondo granite, a late-Variscan pluton (294.3 ± 1.1 Ma; Sergeev & Steiger, 1995) that intruded into the European polymetamorphic crust of the Gotthard nappe (Figure 1a). The granite consists of two magmatic facies, equigranular (Figure 2a) and porphyritic, both with the same mineralogical composition, but with different proportions between felsic minerals and phyllosilicates. Biotite and feldspar foliation occur only in the porphyritic granite (Lützenkirchen & Loew, 2011; Rast et al., 2022). Aplitic and mafic dykes (290–285 Ma; Bussien et al., 2008) crosscut the granite heterogeneously. Deformation throughout the Alpine orogenesis (Alpine metamorphic event) is manifested as a weak bulk foliation in the porphyritic facies of the granite (Steck & Burri, 1971) and more commonly in narrow NE-SW trending ductile shear zones. According to Schmid et al. (1996) the Gotthard massif was backfolded about 20 Ma ago, rotating the tectonic boundaries, the foliation and the shear zones into the actual subvertical setting. Ceccato et al. (2024) identified a sequence of four deformation stages from 34 Ma to present: brittle faulting before the Alpine peak metamorphism; reverse mylonitic shearing at amphibolite facies; brittle-ductile strike-slip shearing

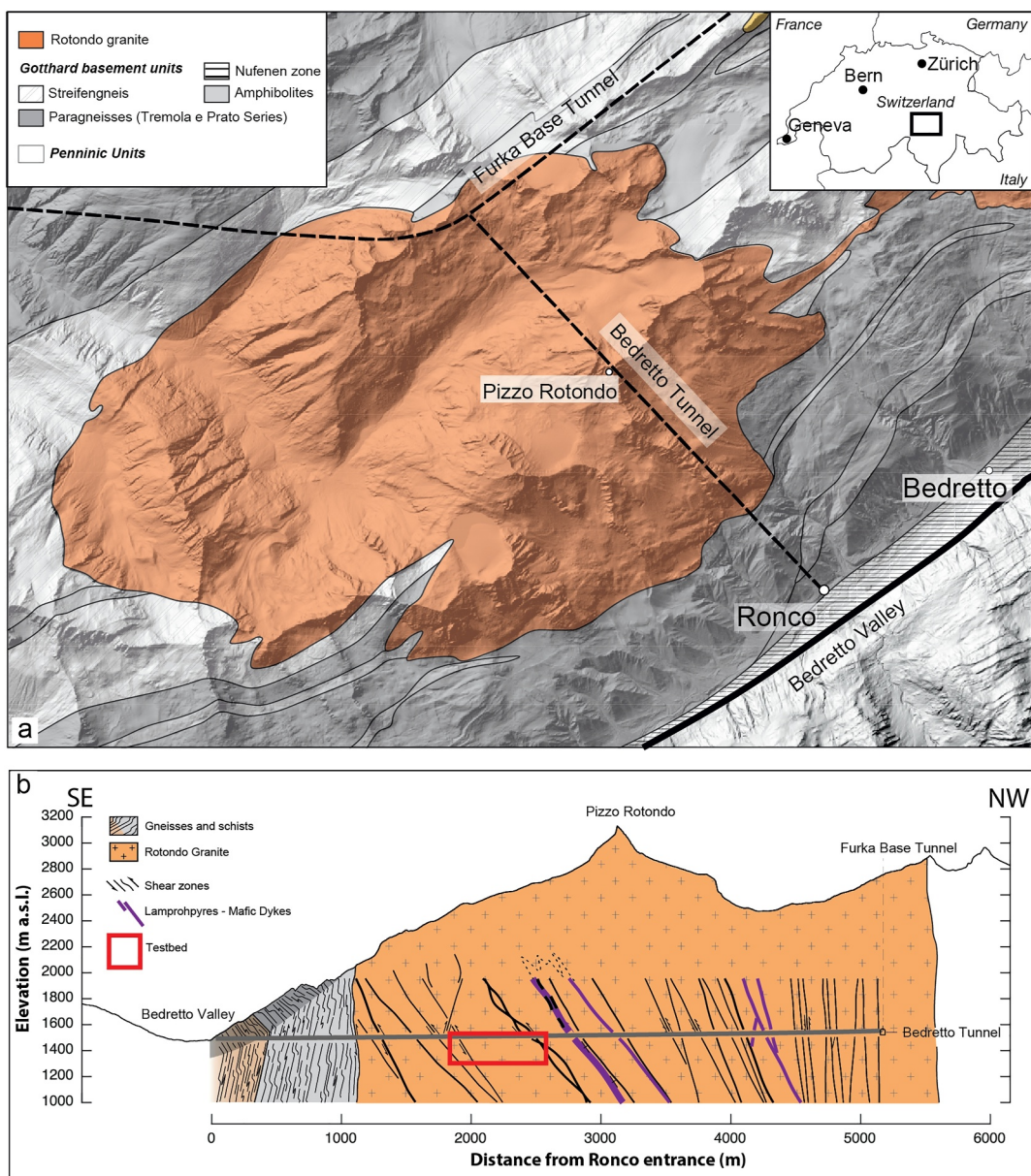


Figure 1. (a) The location of the Bedretto Tunnel in Ticino, Southern Switzerland, a side tunnel of the Furka Railway tunnel. (b) Cross-section of the Bedretto Tunnel with location of the Geothermal Testbed volume, situated 2 km from the Southern entrance of the tunnel, in Rotondo Granite (modified after Ceccato et al. (2024)). The shear zones are only indicative of distribution and geometrical setting of the main structures, and do not correspond to mapped structures.

at greenschist-facies; and brittle strike-slip faulting at shallow conditions. The brittle structures of the first phase controlled the localization of ductile mylonites of the second and following phases, resulting in a large percentage of faults commonly NE-SW oriented.

The brittle faults of the first phase (I) are cataclasites and breccias (Figure 2b) with angular clasts of undeformed granite surrounded by a dark fine-grained matrix. Quartz veins are often associated with these structures. The following ductile shear phase II is manifested by fine grained mylonites with granitic porphyroclasts, sigmoidal quartz and well-developed Bt-foliation (Figure 2c) forming a set of steep, NW-dipping, reverse ductile shear zones (Lützenkirchen & Loew, 2011). The subsequent ductile to brittle phase III is represented by sets of conjugate brittle-ductile strike slip and normal dip-slip faults, N-S or NW-SE oriented, associated with tensional mineralized veins and tensional jogs. Vuggy altered granites (episyenites; Ceccato et al., 2024) are observed close to

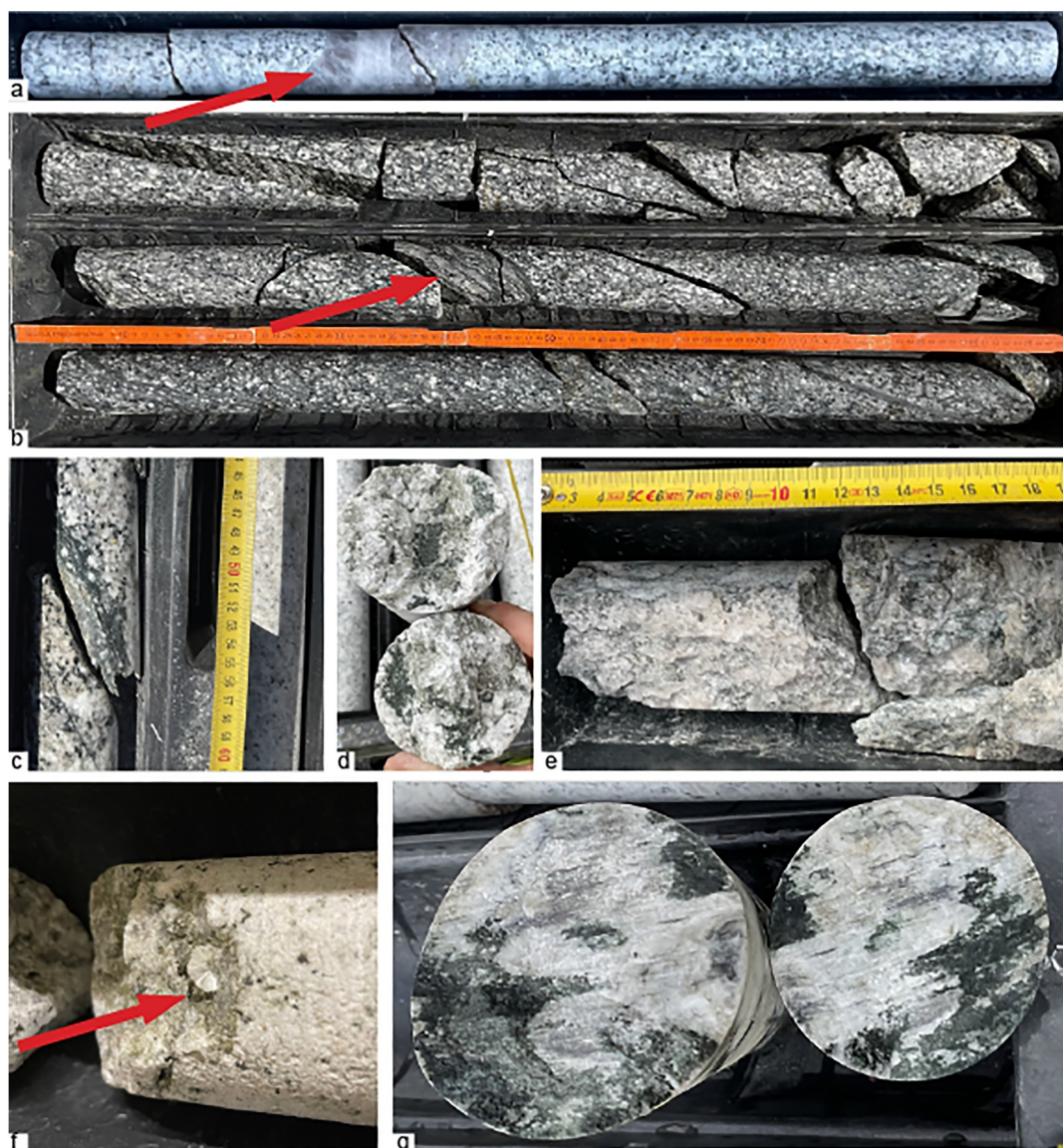


Figure 2. Structures from cores illustrating the various aspects of the Rotondo granite: (a) equigranular undeformed Rotondo granite, crosscut by a Qtz vein (b) breccia with angular clasts surrounded by a dark fine grained matrix, a mylonitic ductile shear zone with highly deformed quartz ribbons; (c) fine grained mylonites with feldspar porphyroclasts, sigmoidal quartz and well-developed Bt-foliation; (d, e) two aspects of vuggy granite with secondary porosity; (f, g) brittle fault plane, characterized by zeolites (arrow in f) and elongated Qtz fibers along the latest movement direction (g).

these shear zones (Figures 2d and 2e). The latest deformation phase IVs represented by NE-SW to E-W brittle faults (Figures 2f and 2g), characterized by zeolites and clay-rich gouges (Ceccato et al., 2024; Lützenkirchen & Loew, 2011). Multiscale remote sensing analyses and field investigations of lineament sets provided insights into the spatial organization, geometry and lateral extent of the four deformation zones. In particular it revealed that the brittle fault zones of phase IV are particularly important, as they are the most laterally continuous at the regional scale. The phase IV brittle shear zones are organized into clusters, with across-strike thicknesses ranging from 2 to 10 m and lateral extents up to several hundred meters (Achtziger-Zupančič et al., 2024). However, these fault zones are composed of discrete and discontinuous shear surfaces and fracture planes, each typically around 50 m in length. Additionally, Type IV brittle fault zones feature zeolite-bearing shear planes, fault mirrors, and cataclasites. These zeolite-bearing fault rocks are widespread in the crystalline basement units of the Alps and are believed to result from past seismic activity associated with (hydrothermal) fluid injection (Ceccato & Pennacchioni, 2018; Dempsey et al., 2014).

Ma et al. (2022) presented a multidisciplinary characterization of the in situ stress conditions and internal structures of the hectometer-scale rock volume, beneath the Geothermal Testbed niche. They found that the rock volume features three distinct compartments, with the middle main fault zone, sandwiched by two relatively intact units. This fault zone unit appears to be a representative feature of the site, as similar structures repeat every several hundreds of meters along the tunnel. Bröker and Ma (2022) determined the far field stress orientations at Bedretto as follows: The maximum principal stress component, S1, has a magnitude close to the overburden stress (≈ 26.5 MPa) and a direction close to vertical (potentially up to 10° inclined). S2 or SHmax has a magnitude between 20.4 and 27.9 MPa and is oriented between N100°–120°E (mean = N112°E). S3 or Shmin is oriented N10°–30°E and has a magnitude between 11.2 and 16.4 MPa. The stress state is not critical at the existing structures (Bröker & Ma, 2022). However, they observed a rotation of the stress field in a counter-clockwise direction by up to 37° in a group of three shallow (30 m) boreholes located inside the lab. This is very likely a local perturbation, but shows that the stress field is very heterogeneous and likely influenced by fractures/fault zones (Bröker, Ma, Zhang, et al., 2024). Through the borehole breakouts in the up to 400 m long monitoring and stimulation boreholes, Zhang et al. (2023) inferred a rotation of the stress field. The rotation is clockwise around the main fault zone and also the relative stress magnitudes change (i.e., the intermediate principal stress moves from S1 toward S3). In addition, the occurrence of the breakouts around the major fault zone indicates a lower rock strength. These observations manifest and highlight the importance of natural and complex rock volumes for experiments aiming to represent natural conditions comparable to shallow (~ 1 km) reservoirs.

From acoustic televiewer (ATV) and optical televiewer (OTV) logs, structures were picked with three main strike directions, NE-SW to E-W, N-S and NW-SE, in line with the geological observations. Fractures can be found in all of these 3 groups, while most fault zone cores are only found in the NE-SW group dipping NW. The identified orientation sets are not distributed equally in the rock volume and the rock volume can be divided in 4 units following structure orientation. N-S directions concentrate in the upper section of the boreholes near the tunnel (Unit I in Figure 3). This is followed by a transition from NS to NE-SW (Unit II, Figure 3) until NE-SW oriented fractures are dominant (Unit III, Figure 3). In Unit IV (Figure 3) the NE-SW set is still dominant, but occurs alongside the NW-SE set. The major fault zone of the Geothermal Testbed marks the boundary between Units II and III.

2.2. Overview of the Injection Intervals

The Bedretto Geothermal Testbed was optimized and conceptually designed to incorporate zone with varying sensor coverage, ranging from high to intermediate and low, for optimal data acquisition. This allows to study effects during reservoir stimulation at a highest resolution, learn to which extent these effects can be monitored from greater distances and, ultimately, transfer this knowledge to full-scale reservoir engineering projects, where only limited resolution by predominantly surface-based monitoring systems is possible. This study presents the results of the uppermost 8 injection intervals of the injection borehole ST1 (Figure 3), located in the region of highest sensitivity/coverage of the monitoring network. Deeper intervals at lower coverage have been stimulated within the DESTRESS project and are partially documented by Giardini et al. (2022).

The ST1 borehole, dipping 49° , is equipped with a 14 interval multipacker system. The experiments described in this manuscript took place in the top 8 intervals that are placed within a dense multi-component monitoring system at depths of 250–50 m below the tunnel (Figure 3). The stimulation intervals are between 7.5 and 54.8 m long (Table 2). Each interval is hydraulically connected to the borehole mouth through sliding sleeve doors (SSD) integrated into the string between the packers. The SSDs serve as injection points and are 1.1 m long. Each SSD is positioned at a depth of 3–4 m below the upper packer of the respective interval. Prior to the deployment of the multi-packer system, a range of logging tools were run in the ST1 borehole to characterize the geological structures therein. We use the acoustic televiewer (ATV) and optical televiewer (OTV) logs to distinguish between filled and non-filled fractures. The latter show clear signatures on the acoustic amplitude and often also travel time images. Note that the fractures that have been identified as non-filled may narrow considerably or terminate a few centimeters or meters away from the borehole. Therefore, it is not possible to assess the continuity of these structures away from the borehole wall and the connection to other structures without constructing an advanced geological model.

In the following, we briefly describe each interval. A complete summary of all technical parameters is given in Table 2. For a full characterization of the intervals, please refer to Bröker, Ma, Doonechaly, et al. (2024).

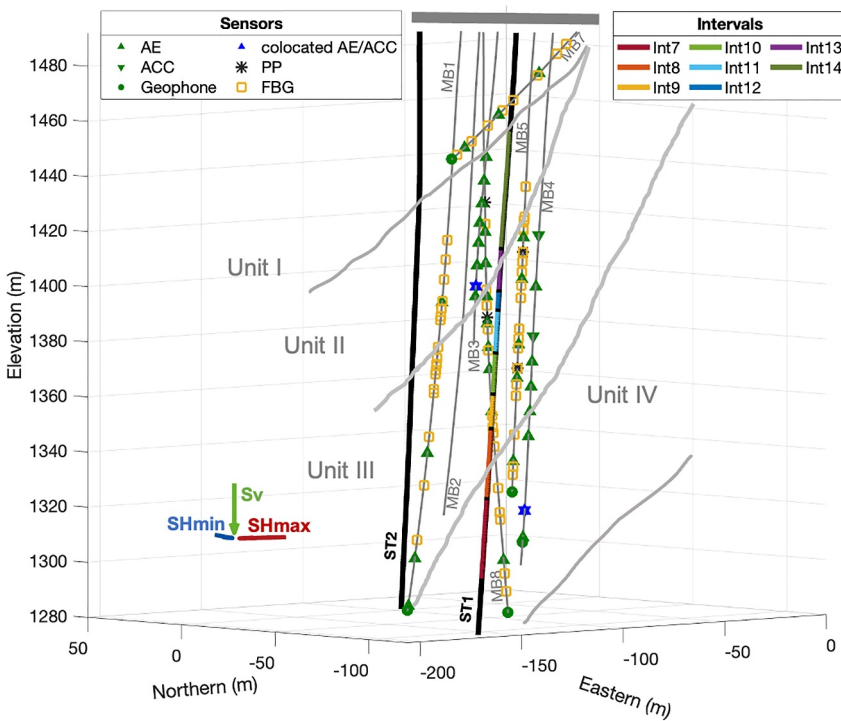


Figure 3. Seismic Instrumentation in the VALTER volume, showing acoustic emission sensors (AE), accelerometers (ACC), geophones, FBG and pore pressure sensors (PP) together with the seven relevant injection intervals. The thick gray line represents the tunnel. In light gray, we roughly delineate the distribution of the main geological units divided by the dominant fracture orientations after Castilla et al. (2022). The uppermost Unit I is dominated by fractures with NS orientations, in Unit II a transition from NS to NE-SW occurs. Unit III is dominated by NE-SW oriented fractures. Toward the bottom of the explored volume NE-SW are still dominant but NW-SE structures are found (Unit IV). The main fracture zone is between Units II and III.

Interval 7 (bottom depth: 253.3, 35.1 m long). The interval contains many filled fractures, undifferentiated fractures (unclear if fracture is filled or non-filled), and two fracture zones from 219 to 221 m. The orientation of these fracture zones is around 240°/60° (strike/dip, “right-hand rule” or RHR) and they have a detectable outflow, as evidenced in the logging data. Because of these structures, the interval is the second most transmissive in the VALTER volume with transmissivity of 3.00E – 7 m²/s (transmissivities are given in Table 2 after Gholizadeh Doonechaly, Bröker, Hertrich, Ma, et al. (2024)).

Interval 8 (bottom depth: 216.8, 30.1 m long). The interval has two prominent non-filled fracture zones from 205 to 207.5 m depth that mark the boundary between Units III and IV (Figure 3). Fractures in this zone strike around 230° and dip between 43° and 60°. In addition, the interval contains many smaller filled fractures and undifferentiated fractures. Despite the large fracture zones, the transmissivity is 3.3E – 8 m²/s and lower than in the neighboring intervals.

Interval 9 (bottom depth: 185.2, 14.4 m long). The interval contains many non-filled fractures with smaller aperture, undifferentiated fractures and a large shear zone. The orientation of the non-filled fractures varies, with an average orientation of 227°/59°. Interval 9 crosscut a prominent ductile shear zone oriented 239°/39° with an apparent thickness of 3 m, associated at the top with brittle fractures with high slip tendency, and at the bottom with a brittle fracture with intermediate slip tendency. Interval 9 has an intermediate transmissivity of 4.1E – 8 m²/s and is more transmissive than its neighboring intervals.

Interval 10 (bottom depth: 169.3, 17.1 m long). The interval contains several smaller non-filled fractures and many undifferentiated fractures. The non-filled fractures are distributed over the entire length of the interval and with an orientation of 231°/69°. The transmissivity is 1.80E – 8 m²/s and relatively low.

Interval 11 (bottom depth: 150.5, 18.3 m long). The interval has multiple non-filled fractures and two fracture zones with an orientation of 233°/58°. The transmissivity is 5.60E – 08 m²/s and higher than in the adjacent intervals.

Interval 12 (bottom depth: 131, 7.5 m long). The interval contains three prominent fracture zones with similar strikes (231°–251°), but different dip angles (49°–80°). The transmissivity is comparably low with 1.90E – 8 m²/s, despite these prominent fracture zones and the proximity to the main fracture zone (interval 13).

Interval 13 (bottom depth: 121.7, 18.3 m long). The interval contains the largest fault zone of the experimental volume that represents the boundary between Units II and III (Figure 3). The major fracture zone in the center of this fault zone extends from around 107.5 m until 113.5 m and is oriented around 240°/69°. Above and below this central fracture zone, several more non-filled fractures, some with a large aperture, are observed. The transmissivity of this interval is by far the highest (8.40E – 7 m²/s).

Interval 14 (bottom depth: 101.9, 54.8 m long). The interval only contains two non-filled fractures, oriented 237°/63°, and is mostly intact rock with many filled fractures. The transmissivity is low with 2.30E – 9 m²/s.

2.3. Multi-Parameter Monitoring Network

We encountered various challenges in the design of a high-resolution multi-component monitoring network for meso-scale experiments. One challenge regards the substantial deviation in borehole drilling for 400 m long boreholes (for details see Plenkers et al., 2023). The exact design of the network could only be finalized, once the final trajectories were known. Since drilling long boreholes was expensive, the total number of boreholes was limited and each of them needed to accommodate various types of sensors. Water and pressure at depth in the boreholes were an additional challenge, in particular for electronic parts such as preamplifiers. The extensive development efforts and final sensor types are described in detail in Plenkers et al. (2023). An additional challenge for the seismic monitoring system during the VALTER stimulations was that we aimed to cover a wide range of seismic signals. We wanted to record induced seismic events down to $M_w < -4$ (pico seismicity), with frequencies up to 100 kHz and at the same time record low-frequency signals (0.08–100 Hz) observed in previous in situ stimulation experiments (Boese et al., 2022; Zang et al., 2017) that are speculated to represent aseismic, pressure-driven deformation. Since no seismic monitoring system covers the recording of this wide range of seismic signals, we installed three different seismic systems using (a) strong motion/broadband seismometers along the tunnel; (b) geophones; (c) high-frequency 3-component accelerometers (ACC) and acoustic emission (AE) sensors in the boreholes (Figure 3). For the observations reported in this article the borehole ACC and AE sensors are the most relevant, and are referred to from here on as ultra-high frequency network.

Instrumenting the experiment volume was challenging and followed a sophisticated installation concept (Plenkers et al., 2023). As expected, due to the risks involved in instrumenting a multi-sensor network in such an environment on meso-scale, sensor failure occurred. The ultra-sensitive AE sensors and accelerometers that come with internal electronics in the sensor's preamplifiers were especially affected. A prolonged exposure to borehole water in between installation and cementation (MB1 and MB4), was identified as a risk factor. For later installations, the installation procedure was revisited and the exposure time in the open boreholes was reduced to a minimum, which successfully reduced the number of failed sensors.

For VALTER, we used the following sensors installed in six 100–300 m long monitoring boreholes (MB1, 3, 4, 5, 6, 7, Figure 3): 5 triaxial geophones type IMS-GS-100 Hz, an ultra-high frequency network that incorporates 5 triaxial accelerometers (ACCs) type IMS-3A25 and IMS45A19, 34 Acoustic emission (AE) sensors type GMuG-Ma-Blc-30-35, 12 ultrasonic transmitters GMuG-Blc-Tr50 and GMuG-Blc-Tr70. Further we have 4 cementable tube pore pressure (PP) sensors, 58 FBG sensors and optical fibers for the measurements of temperature, strain and acoustic emissions in all boreholes. More detailed specifications of the sensors can be found in Plenkers et al. (2023).

The ACCs were collocated with AE sensors to allow for their cross-calibration (briefly outlined in Section 3.3). We used two types of ACC, a Wilcoxon sensor with a flat response between 2 Hz and 25,000 Hz (± 3 dB) and an Endevco sensor with a narrower flat response but higher sensitivity, between 0.5 and 3,000 Hz. AE sensors used were tailored toward a reduced resonance and optimized for the frequency range 1–50 kHz. Above 50 kHz the sensor's sensitivity is reduced, but signals are recorded. The upper limit of high-frequency recording at 100 kHz is defined in this project by the sampling frequency. The sensor's directivity is highest in borehole direction and

slightly reduced but constant in radial direction. The six monitoring boreholes were all sealed on their full length with a fit-to-purpose cementation (Gholizadeh Doonechaly, Reinicke, et al., 2024; Plenkens et al., 2023) to minimize their impact on fluid pathways and hydrogeological conditions of the experimental volume. Additionally, we have a 222 m long open monitoring borehole (MB2) equipped with a classical multi-packer that isolates 7 intervals between depths of 125 and 222 m, ranging in length from 1.5 to 22 m. The uphole pressure can be read for the corresponding intervals at the surface. For injection and production, we have a 404 m long injection borehole (ST1) with a 14 interval multipacker system (the intervals are described in Section 3.1 and in detail in Bröker, Ma, Doonechaly, et al. (2024)) and ST2, a 351 m long borehole that shall be used for fluid circulation (production) at a later stage.

2.4. A-Priori Risk Study, TLS, and ATLS

For the BedrettoLab, we performed an a-priori probabilistic risk assessment to assess potential hazard and damage in the Bedretto and Furka tunnels, as well as for infrastructures and buildings on the ground surface. Such a risk study is a common and useful practice to manage and mitigate induced seismicity linked to injection activities in the underground (Broccardo et al., 2020; Grigoli et al., 2017). The analysis was performed for a range of possible injection volumes, ranging from 1 to 1,000 m³. Since the specific site response was unknown prior to the injection activities, we relied on a range of models and model parameters available in literature. Prior information from other representative sites, including some at industrial scale, for example, Basel and St. Gallen in Switzerland (Diehl et al., 2017; Häring et al., 2008), Pohang in South Korea (Grigoli et al., 2017), Soultz-sous-Forêt in France (Horálek et al., 2010), as well as other underground laboratories (Grimsel in Switzerland (Villiger et al., 2020, 2021), Äspö in Sweden (Zang et al., 2020)), was accounted for via expert rating (Gischig et al., 2019). The a-priori analysis was updated as new data from the stimulations became available.

The a-priori analysis also describes the thresholds for a traffic light system (TLS) and the actions to be taken (from bleed-off to tunnel evacuation) if a given alert level is reached. We implemented two completely independent monitoring systems for the TLS to monitor the safety of the operations, (i.e., with stations that do not share data and network). The first system (vibration-based TLS or TLS-V) is based on direct ground motion recording at three surface accelerometers located in the tunnel niche of the Bedretto Geothermal Testbed (few tens of m from the injection borehole head). The thresholds for ground motion are fixed at 0.5, 2.5, and 15 mm/s for yellow, orange, and red alerts, respectively. The second system is based on recorded earthquake magnitudes (TLS-M). The thresholds are based on potential median ground motion and hence also dependent on injection depth and the distance between the earthquake location and the stimulated reservoir. For the injection activities described in the current work, TLS magnitudes were taken from the AE detections during active injection operations, and from a geophone-based background network for all other periods. For the shallowest interval 14 at about 50 m distance from the Bedretto Tunnel, the magnitude thresholds are as low as $M_w - 1$, $M_w 0$, and $M_w 1$ for yellow, orange, and red alerts, respectively. For the deepest intervals with a distance of more than 300 m from the Bedretto Tunnel, the thresholds are $M_w 0.5$, $M_w 1.5$, and $M_w 2.5$ for yellow, orange, and red alerts, respectively. Details for the magnitude thresholds for the injection activities can be found in Table 1. During the simulations, the yellow TLS alert was reached two times: the first during the joined stimulation of Intervals 9/10 in Phase 2A, and a second time—intentionally—for the Interval 10 Phase 2B stimulation. A posteriori analysis of the data, however, showed that the real-time MI magnitude was overestimated compared to the M_w of the event triggering the threshold level.

For research purposes, we recursively tested an Advanced Traffic Light System (ATLS) in real time, referred to as RT-RAMSIS (Real Time Risk Assessment and Mitigation for Induced Seismicity, <https://gitlab.seismo.ethz.ch/indu/rt-ramsis>). Both real-time seismic and hydraulic data (injection flow rate and pressure) feed the software, which forecasts the seismicity rates for the next activities. Seismicity rates were computed following a simplified model (Broccardo et al., 2017; Mignan et al., 2017). Potentially hazardous conditions could then be estimated from the simulated seismicity rates following standard approaches (e.g., OpenQuake, Pagani et al., 2014). Given the probabilistic-based approach, the thresholds for an ATLS are reported as the probability of exceeding a 30 mm/s peak ground velocity, with values at 1/1,000, 1/100, and 1/10 for yellow, orange, and red alert, respectively.

Table 1

TLS-V and TLS-M Thresholds During Stimulation Activities

Depth (m)	Green (less than)	Yellow (greater equal)	Orange (greater equal)	Red (greater equal)	Comments
TLS-V	0.5 mm/s	0.5 mm/s	2.5 mm/s	15 mm/s	
TLS-M	>50	-1	-1	0	1 Interval 14
	>100	-0.5	-0.5	0.5	1.5 Intervals 11-13
	>150	-0.15	-0.15	0.85	2 Intervals 9-10
	>200	0.15	0.15	1.1	2.15 Intervals 7-8
	>250	0.35	0.35	1.3	2.35 Interval 6
	>300	0.5	0.5	1.5	2.5 Intervals 1-5

Note. M_w corresponds to the median ground motions of 0.5, 2.5, and 15 mm/s at the given distance/depth to the interval.

2.5. Stimulation Concept

We applied a two-phase approach for the development of the model geothermal reservoir, that is, a “characterization phase” followed by a “reservoir engineering phase.”

In the first phase (phase 1), the *characterization phase*, we visited each interval with a standardized injection protocol to compare the influence of the targeted geological structures to the seismo-hydromechanical response (Figure 4a). This characterization phase ties into the strategy applied at the Grimsel Test Site, where standardized stimulation protocols (including nearly constant volume) were employed to observe the interval-specific response and its geology-dependent variability (Krietsch et al., 2020; Villiger et al., 2020). The response of the different intervals provides essential information to decide on further stimulation approaches in the second phase.

Table 2

Overview of the Hydraulic Stimulation Experiments Sorted by Interval and Injection Phase

Interval/Phase	Interval length (m)	Injection depth below tunnel (m)/Local coordinates	Date (DD/MM/YY)	Total injection time (hr)	Injected volume (m ³)	Reactivation pressure (MPa) (cycle 1, cycle 2)	Transmissivity before stimulation (E – 8 m ² /s)	Transmissivity after stimulation (E – 8 m ² /s)
7/1	35.1	236.36/1,312	17/11/21	~4	14.1	10.5, 11.5	30	23
8/1	30.1	203.56/1,337	09/02/22	~3	4.8	13.4	3.30	23
8/2A	30.1	203.56/1,337	22-23/06/22	~32	273.8	14.5, 15.4	28	110
9/1	14.4	180.35/1,355	16/02/22	~6	1.3	14.2, 13.1	4.10	2.3
10/1	17.3	161.17/1,369	02/03/22	~4	1.1	11.7, 13.2	1.80	1.5
9-10/2A	31.7	170.76/1,362	15-16/03/23	~16	54.0	13.0, 14.1	7.6	15
11/1	18.3	142.88/1,382	09/03/22	~8	2.2	15.3, 13.3	5.60	4
11/2A	18.3	142.88/1,382	19/04/23	~10	6.0	14.7	9.3	12
11/2B	18.3	142.88/1,382	12/07/23	~5.5	6.2	–	13	21
12/1	7.5	128.61/1,393	16/03/22	~3.5	0.3	–	1.90	1.2
12/2A	7.5	128.61/1,393	6-7/07/22	~10	2.4	16.4, 18.0	–	9.7
12/2B	7.5	128.61/1,393	28/02-02/03/23	~7	2.9	17.6, 18.0	–	–
13/1	18.2	112.91/1,404	23/03/22	~3	12.9	–	84	78
14/1	54.8	75.87/1,431	03/22	~3.5	1	10.2, 9.6	0.23	5.6

Note. We shaded Phase 1 stimulations in gray. Reactivation pressure and transmissivities are taken from Bröker et al. (2023), Bröker et al. (2024), Gholizadeh Doonechaly et al. (2023), Gholizadeh Doonechaly, Bröker, Hertrich, Ma, et al. (2024), and Gholizadeh Doonechaly, Bröker, Hertrich, Rosskopf, et al. (2024).

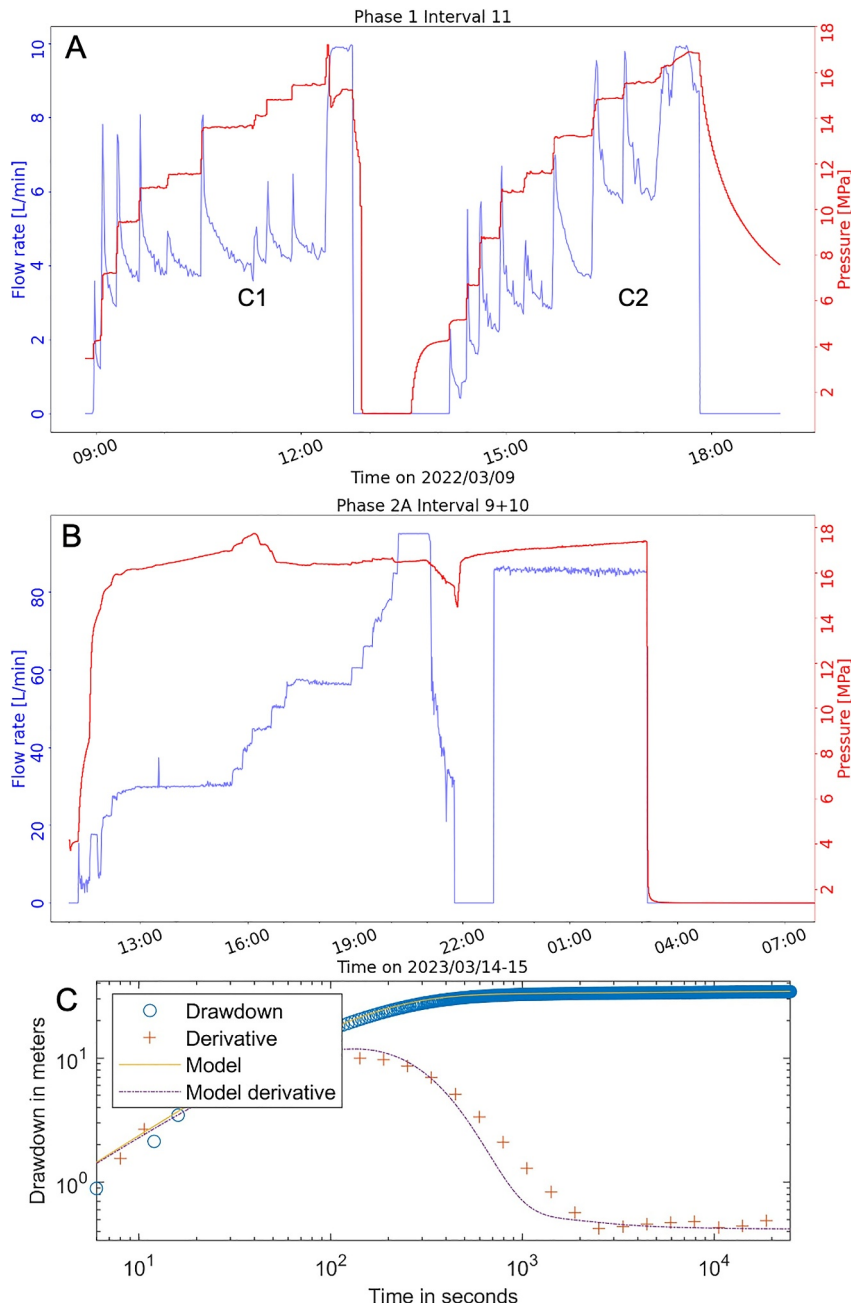


Figure 4. (a) A representative injection protocol for the characterization phase (phase 1 stimulations) showing two pressure-controlled injection cycles. (b) An exemplary injection protocol for the reservoir engineering (phase 2 stimulations). (c) An exemplary constant rate pumping test in interval 12. Shown are the pressure change profile and its derivative.

The injection protocol consisted of two injection cycles (C1, C2, Figure 4a), in which either the injection pressure (interval 8, 9, 10, 11, 12, 14) or flow rate (interval 7, 13) was increased in a stepwise manner after quasi-steady state conditions, that is, constant pressure and flow rate, were reached. In C1, we determined the approximate range for the reactivation pressure, which was refined in C2 using smaller increments in pressure/flow rate. The reactivation pressures are determined from pressure versus flow rate (P-Q) plots, as detailed in Bröker, Ma, Doonechaly, et al. (2024).

In most cycles, the last injection step was extended, followed by a shut-in phase, where injection was stopped, and a venting phase, in which the pressure in the injection-interval was bled off. In between the two cycles, we also

shut-in. Between 0.3 and 14.1 m³ of fluid volume were injected during this phase (Table 2). Prior to each stimulation experiment, we performed a hydrotest, during which typically no seismicity was recorded. Depending on the transmissivity of the interval, different types of hydrotests were carried out, including constant rate pumping test, constant head test, or pulse test (Figure 4c). The hydrotests were designed to have a maximum pressure change in the interval in the order of 1 MPa. The constant flow hydrotests were analyzed with the Hytool software (Renard, 2017) based on Papadopoulos and Cooper (1967). The results were used to estimate the influence of the stimulations on the transmissivity of the intervals of interest.

In a second phase (phase 2), the *reservoir engineering phase*, we revisited intervals once (phase 2A) or twice (phase 2B) to explore effects of upscaling in terms of injection volume or of different stimulation approaches (an example is shown in Figure 4b for the joint stimulation of intervals 9 + 10). A future third phase (phase 3) shall be dedicated to circulation experiments (fluid, heat) in the context of *reservoir management*. Injection protocols for all stimulations can be found in Supporting Information S1 (phase 1), S2 (phase 2A), S3 (phase 2B).

Interval 8 was stimulated with nearly two orders of magnitude larger volume (274 m³ compared to 4.8 m³ in phase 1) to investigate how stimulation reaches beyond the previously stimulated zone and if it connects with the fracture network stimulated from other intervals of phase 1 or to the other boreholes. Interval 8 was chosen for this as it showed abundant seismicity that expanded laterally for over 50 m in phase 1. Also, the transmissivity was substantially changed by the phase 1 stimulation. With similar objectives, the intervals 9 and 10 were jointly stimulated with much larger volume (54 m³ compared to 1.1–1.3 m³ in phase 1). Interval 9 and 10 seemed to show a fluid pathway connection in phase 1, with seismicity occurring in the exact same volume and pressure reacting strongly in the respective other interval. In Interval 11 and 12 the effect of preconditioning prior to stimulation, as well as cyclic stimulation was tested. The idea was to modify the driving stresses around the injection borehole above the clamping stresses to induce seismic slip in the form of a single, larger event (Ellsworth, 2013). For this purpose, two scenarios were tested: In phase 2A, the fluid pressure was increased by injecting several hours close but below the reactivation pressure. In phase 2B, we manipulated shear stresses via cycles of depletion and rapid injection. Further, the effect of stimulation on microbial and geochemical observations was tested in the Interval 11B experiment. Additionally, these phase 2 injections in the intervals 11 and 12 at similar volumes as in phase 1 allowed investigating the repeatability of seismic patterns in terms of reactivation pressure and spatial distribution. Injection protocols for all stimulations can be found in Figures S1–S3 of the Supporting Information S1.

3. Seismic Data Processing

3.1. Data Acquisition With DUGseis in Pseudo Real-Time

With sensors of the ultra-high frequency network, we recorded passive ground motion in the frequency range from 50 Hz to 100 kHz. Continuous waveforms were recorded from 34 AE sensors and for 12 ACC components at a sampling rate of 200 kHz. The recording typically started a few hours prior to the experiments and was kept running for a handful of days afterward. Data was directly streamed to a server at ETH Zurich. One seismic acquisition system (DAQ) with 32 channels at 200 kHz sampling rate and the conversion to the compressed Adaptive Seismic Data Format (ASDF; Krischer et al., 2016; Villiger et al., 2020) produced about 470 GB data per day. For accurate timing in the sub-microsecond range of the different seismic recording system we relied on GPS controlled triggering and clocking. At peak times, when we had 4 recording systems, ultrasonic transmitters and all other sensors/fiber recordings running, we streamed 1.5 TB per day, which is a logistical challenge. The ASDF format allows for flexible and fast access to the data and is integrated in an open-source Python library for seismology (ObsPy) that is also used for event detection. We perform a first-order processing in pseudo real-time using the python-based Dugseis software (Rosskopf et al., 2024a) that was developed locally for the processing of pico-seismicity. We call it “pseudo real-time,” since the ASDF files need to be written first, before they are accessed for processing. This adds a delay in the order of the file length, in this case 10 s. For the processing, we used a homogeneous velocity model with a P-wave velocity of V_p = 5.4 km/s and an S-wave velocity of V_s = 3.1 km/s. These values were obtained averaging cross-hole seismic data and could be confirmed with time-distance plots from pico-seismic data (Figure 5a). The seismic events exhibit clear P- and S-wave arrivals (Figure 5a). Depending on the station location, medium to strongly scattering P- and S-coda wave trains can be observed (Figure 5a). Local attenuation effects are likely also responsible for the delayed S-waves at some station locations. In Figures 5b and 5c, we plot the power spectral densities for various events ranging from M_w = −4.87 to −2.29 at a close distance of 16 m (B) and at a larger distance of 80 m (C). All signals are clearly above the noise

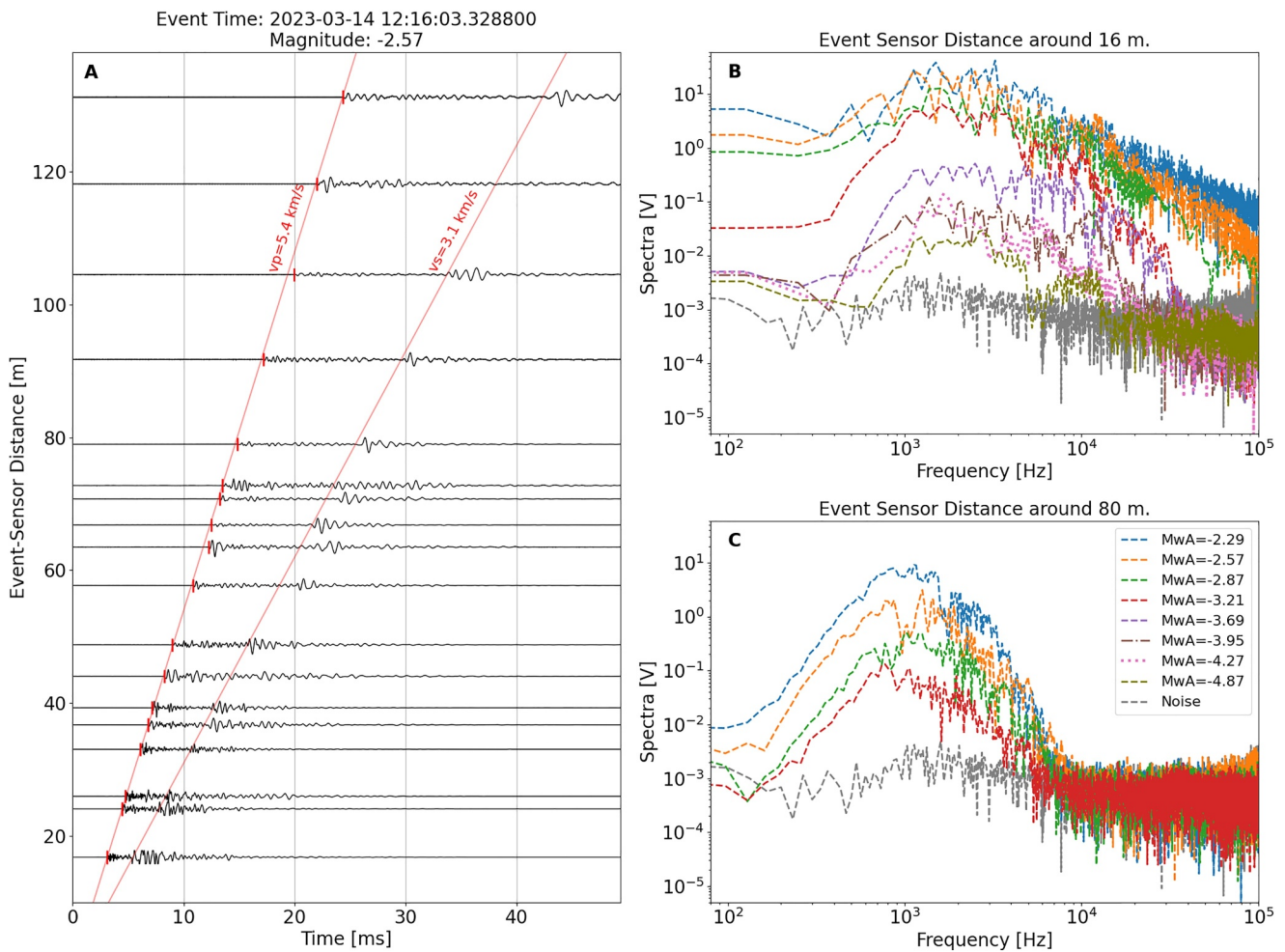


Figure 5. (a) An exemplary seismic record from a $M = 2.57$ shows clear recordings of P- and S-phases and velocities of 5.4 and 3.1 km/s, respectively. (b) Power spectral plots in Volt uncorrected for instrument response, radial spreading and intrinsic damping for various events ranging from $M_w = -4.87$ to -2.29 at a close distance of 16 m and (c) a larger distance of 80 m. We can clearly observe the loss of high frequency energy at larger distances.

(gray line in Figures 5b and 5c). We observe the loss of high frequencies $>5 \text{ kHz}$ due to intrinsic damping at distances of 80 m for all event magnitudes.

3.2. Seismic Event Detection and Location

We process the data in three individual processing runs: (a) a quick real-time processing using the STA/LTA method including a coincidence trigger associator on the five stations closest to the stimulation interval to monitor the generated seismicity during the stimulation to be able to raise an alert if the magnitude of an event exceeds a given threshold (determined in advance for each stimulation interval, see the adaptive traffic light system described in Section 2.4) and give the operator the possibility to react. (b) A more precise fully automatic pseudo-real-time processing using a multi-frequency bands kurtosis (FBKT) picker (Poiata et al., 2016). A filter-bank of 5 logarithmically spaced filters in the range of 2, 25–100 kHz was used to compute the characteristic Kurtosis function. This step refines the locations and the magnitudes of the events during the ongoing stimulation to have a better image of the spatio-temporal evolution of the seismicity. (c) A post-stimulation processing to extract a very precise seismicity catalog (HQ, for high quality) that is used for more in-depth analysis. Here, the STA/LTA picker is again applied to the 5 closest stations to the stimulation interval detecting potential event candidates. At the times of event candidates, an FBKT picker is applied to all recorded AE sensor waveforms. Additionally, we

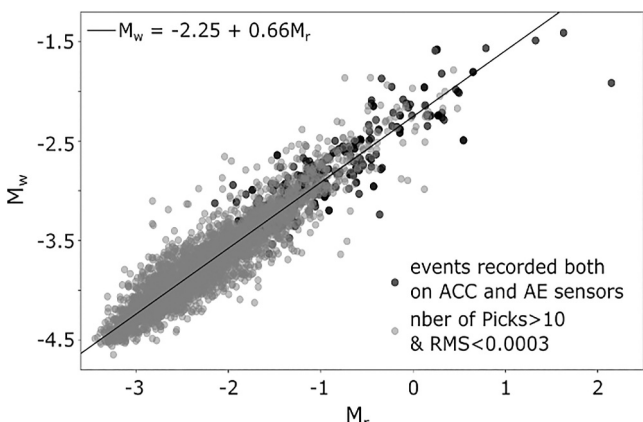


Figure 6. Relationship between the relative magnitudes M_r and the moment magnitudes estimated from the fit of the velocity spectra. The black dots are for the events recorded both on accelerometer ACC and acoustic emission AE sensors. The gray dots are the best events recorded on AE acoustic emission sensors, located with a high number of P-arrival times (Picks) and a small time residual (RMS).

apply an autoregressive–Akaike information criteria (AR-AIC) picker (Bagagli, 2021; Leonard & Kennett, 1999; Maeda, 1985) that substantially improves the picking quality. For the presented catalogs, only P-picks were used. S-picks in general increase the accuracy but have no significant effect in this setting due to the three-dimensional coverage with sensors (Rosskopf et al., 2024b).

Events were located in an absolute way using a homogeneous background medium with $V_p = 5.4$ km/s (Section 3.1). Uncertainties in the absolute event location can arise from uncertainties in the borehole trajectories (Plenkers et al., 2023), and the picking of the P-arrival times. To reduce these uncertainties, a relative relocation was performed using a double difference event relocation method, applied directly to the catalog picks without cross-correlation (Scarabello & Diehl, 2021; Waldhauser & Ellsworth, 2000). The double difference relocation reduces the number of outliers and improves the clustering, while losing less than 3% of the events. As a last step, the largest events in the HQ catalogs are manually revised, repicked if necessary, and relocated. A more detailed description of the processing and challenges encountered can be found in Rosskopf et al. (2024b), and final HQ catalogs with and without relative relocation in Rosskopf et al. (2024c).

3.3. Magnitude Computation

In experiments producing pico-seismicity, one key challenge is to compute magnitudes from the highly sensitive, but uncalibrated, AE sensor recordings (e.g., Manthei & Plenkers, 2018). The lack of calibration means that no instrument response is available to correct the recorded signals from the complex instrumental response and compute an absolute moment magnitude (M_w). Following the procedure from Plenkers (2010) and Kwiatek et al. (2011), we used two ACCs located in the central part of the stimulated volume and collocated AE sensors (marked in blue in Figure 3) to extract by deconvolution a calibration function for all AE sensors (Figure S4 in Supporting Information S1) and gain instrument corrected velocity spectra. We use a grid search approach following Kwiatek et al. (2011) to fit theoretical spectra assuming the source model of Boatwright (1978) to estimate the source parameters; seismic moment, corner frequency and quality factor Q_c of events with a corner frequency within the accelerometer range below 20 kHz. This enables us to use the standard relation from Hanks and Kanamori (1979) to estimate absolute moment magnitudes M_w . We gain magnitudes for smaller events by calculating relative amplitude magnitudes M_r . We then use the absolute M_w to adjust the relative amplitude magnitudes M_r to a realistic magnitude level. Following the procedure from Kwiatek et al. (2011) we obtain

$$M_w = -2.25 + 0.66M_r \quad (1)$$

This relationship holds over at least three orders of magnitude, and is considered robust (Figure 6).

We estimated source parameters for 468 events. The absolute spectra-derived moment magnitudes of these events ranged from $M_w = -3.2$ to $M_w = -1.6$. Assuming the circular source model of Madariaga (1976), the estimated corner frequencies suggest source radii of cm-size and a static stress drop around 1 MPa. Amplitude based moment magnitudes M_w could be derived by regression analysis for the entire catalog and incorporate smaller magnitudes ranging from $M_w = -4.5$ to $M_w = -1.6$.

4. Results

In this section, we show the results from the seismic analysis. We first discuss the network performance, and then focus on geometric features, the relationship of seismicity to injection volume and pressure, and statistical properties. We also summarize relevant observations from other sensors of our multi-component monitoring network, such as pressure and strain. Details on the processing of these data sets can be found in Bröker, Ma, Doonechaly, et al. (2024) and Gholizadeh Doonechaly, Reinicke, et al. (2024).

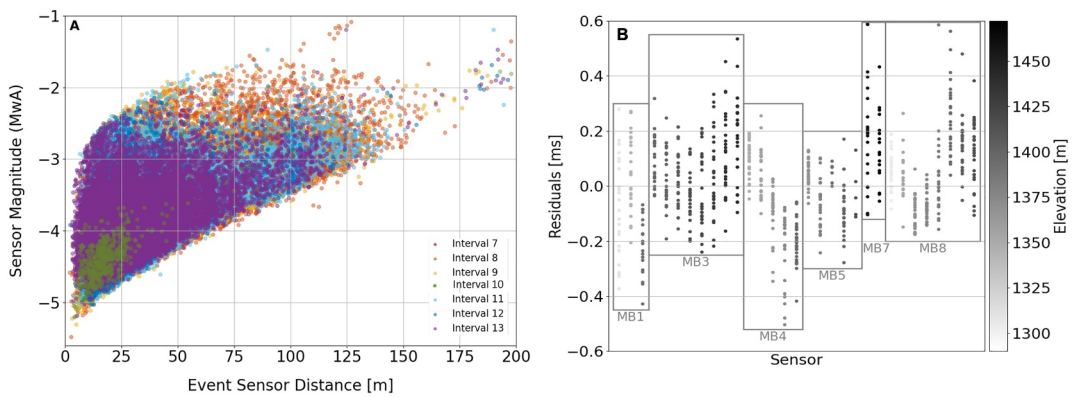


Figure 7. (a) Detected magnitudes on single sensors with event-sensor distance for events from all stimulation intervals show a linear trend for distances larger than 15 m. (b) Station residuals for the 27 largest events recorded during the phase 2 stimulation in int9/10, at a central location in the monitoring volume. The sensor residuals are sorted by borehole and color-coded by sensor depth.

4.1. Seismic Network Performance

To gain an understanding of the spatial variability of our network sensitivity, we looked at the sensor magnitude with event-sensor distance (Figure 7a), the station travel time residuals (Figure 7b) and the distance of a specific location in the volume to the nearest sensors as a direct proxy of the detection sensitivity (Figure 8).

The single sensor magnitude follows a linear relationship with event-sensor distance for distances larger than 15 m (Figure 7a). As an example, at distances of 15 m, we can detect magnitudes of $M_w = 4.95$ and at distances of 50 m $M_w = 4.3$. The very near field (< 15 m) seems to follow a slightly steeper slope. We computed the location residuals for individual sensors for the 27 largest events recorded during the phase 2 stimulation in int9/10, at a central location in the monitoring volume. They are well centered around 0 (Figure 7b). However, there is a slight residual increase for sensor positions above 1,400 m in MB3, MB7, and MB8, as well as for deep sensor positions in MB1 and MB4. The residual increase at shallow depth is likely linked to the crossing of the main fault zone that increases rock anisotropy. The larger residuals for sensors at depth could be linked to uncertainties of the borehole trajectory that increases with depth and can reach as much as 1 m at the bottom of the boreholes.

To evaluate the network sensitivity, we divided the stimulation volume in grid cells of $1 \text{ m} \times 1 \text{ m} \times 1 \text{ m}$ and computed the distance from each grid cell to the 5th nearest sensor (Figure 8a). We chose the 5th sensor since an event needs five detections to be considered a candidate for the HQ catalog. In the central part of the volume around injection intervals 9, 10, 11, and 12, the 5th sensor is within less than 10 m. Here, we expected the highest

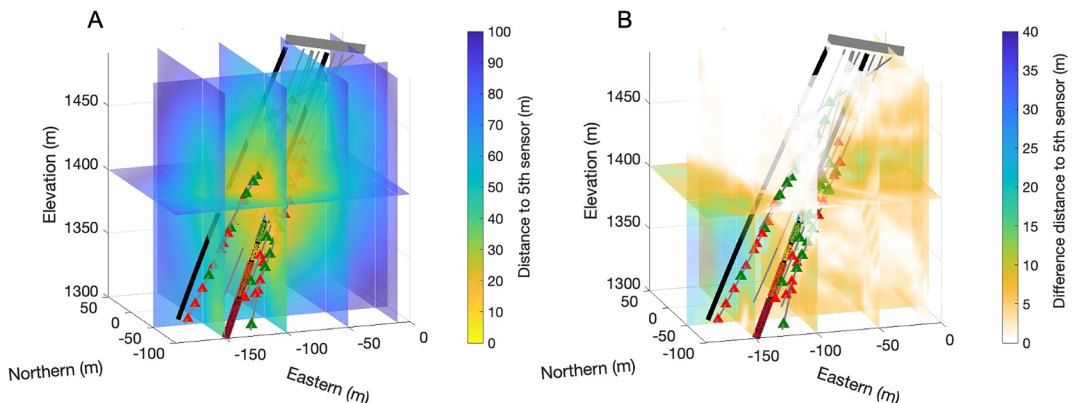


Figure 8. (a) Network sensitivity expressed as the distance to the 5th sensor for the functional network (green). (b) Difference in distance to the 5th sensor between the planned (green and red sensors) and functional network (green). An increase of up to 40 m is noticeable in the lower northern part of the volume, reducing the detection capacity of small events in this region. The injection intervals are color-coded as in Figure 3.

Table 3

Overview of the Seismic Responses to the Hydraulic Stimulation Experiments Sorted by Interval and Injection Phase

Interval/ Phase	Number detections	Number of HQ events	<i>N</i> of events above M_c	<i>N</i> events after shut- in ($>M_c$)	Max M_w	Lateral extent of seismically activated volume (m)	(Concentric) growth of seismicity	Seismic activation pressure (first 5% of events)	<i>a</i> -value of GR law	<i>b</i> -value of GR law	Seismogenic index (a_{jb})	
7/1	398	254	179	22 (12%)	-2.6	90	No	9.82	-4.20	-2.57	1.15	-3.85
8/1	2,080	1,289	563	32 (6%)	-2.84	55	Yes	13.82	-4.04	-7.15	2.45	-7.88
8/2A	12,776	9,369	5,678	201 (3.5%)	-1.64	130	Yes	15.06	-4.14	-0.80	1.10	-3.28
9/1	832	567	243	17 (7%)	-2.98	30	No	15.46	-4.48	-8.14	2.35	-8.33
10/1	922	611	434	17 (4%)	-3.48	30	No	12.63	-4.58	-7.58	2.23	-7.48
9-10/2A	7,086	6,002	3,867	233 (6%)	-2.29	55	Yes	15.24	-4.19	-2.40	1.43	-4.20
11/1	99	98	63	4 (6%)	-2.75	30	No	13.49	-4.25	-4.70	1.53	-5.08
11/2A	4,087	3,848	2,174	62 (3%)	-2.39	35		15.24	-4.29	-3.31	1.55	-4.18
11/2B	5,310	4,615	2,741	243 (9%)	-2.24	40		18.64	-4.14	-2.07	1.33	-2.93
12/1	241	233	164	1	-2.42	7	No	10.33	-4.42	-1.98	0.95	-1.55
12/2A	500	420	236	0	-2.27	15	Yes	17.99	-4.37	-3.43	1.33	-3.80
12/2B	683	599	299	2	-2.55	8		17.52	-4.35	-4.83	1.68	-5.30
13/1	5,146	2,417	1,295	85 (6.5%)	-2.31	40	Yes	6.17	-4.11	-1.82	1.20	-2.98
14/1	460	204	87	0	-4.02	25	No	10.93	-4.42	-10.57	2.83	-10.55

Note. We shaded Phase 1 stimulations in gray.

sensitivity to events as small as $M_w - 5$ (Figure 7a). At distances of 50 m to the 5th sensor (intervals 7, 8, 13), we can still expect a sensitivity to events of $M_w - 4.3$. Toward the outer parts of the volume of interest, at distances of 70–80 m (interval 14), we are sensitive to $M_w - 3.8$. A comparison between the originally planned network (Plenkers et al., 2023) with the functional network reveals that we have reduced coverage at depth, toward the north (Figure 8b). Due to the sensor failures, especially in borehole MB1, the distance to the 5th sensor is increased by up to 40 m, which results in a reduction in detection sensitivity of about 0.5 magnitude points. Determined by the network geometry, events occurring outside of the central volume have a limited azimuthal coverage.

For large events, the AE sensors clip amplitudes for $M_w - 3.0$ at distances closer than 20 m and for $M_w - 2.4$ at distances closer than 40 m. Since the seismic network extends over 150 m, we have still had more than 10 unclipped recordings for our largest events with $M_w > -2.0$. To be able to record and locate even larger events, we have the borehole bottom geophones in place that recorded about 850 events during all stimulations. The smallest events recorded on the geophones have roughly estimated magnitude of $M_w - 3$ at a distance of 30 m.

4.2. Spatio-Temporal Properties of Seismic Clouds

In the following, we describe the spatio-temporal patterns of the seismic clouds for the individual intervals for phase 1 and 2. The key numbers are also summarized in Tables 2 and 3. In Figures 8–11, we show the spatio-temporal evolution of the seismicity for the various stimulations on a plan view (for details on the view, see Figure S5 in Supporting Information S1). The Figures are arranged to allow discussions of interesting features and by interval number. An animated 3D representation for each experiment is embedded in the online version of this article.

Interval 7 (phase 1: 398 detected events, 254 HQ events). Seismicity was quite scattered with a lateral extent of 90 m and no clear alignment along planes (Figure 12a). Sensor coverage in this interval is reduced.

Interval 8 (phase 1: 2,080 detections, 1289 HQ events; phase 2A: 12,776 detections, 9369 HQ events). Seismicity in phase 1 extended over 55 m and was mainly located at the upper part of the interval, moving toward ST2 (Figure 9a). Interval 8 showed a strong mechanical connection to deeper parts of MB1 and MB5 during the characterization phase. We observed a seven-fold increase in transmissivity, reaching $23 \times 10^{-8} \text{ m}^2/\text{s}$. During the

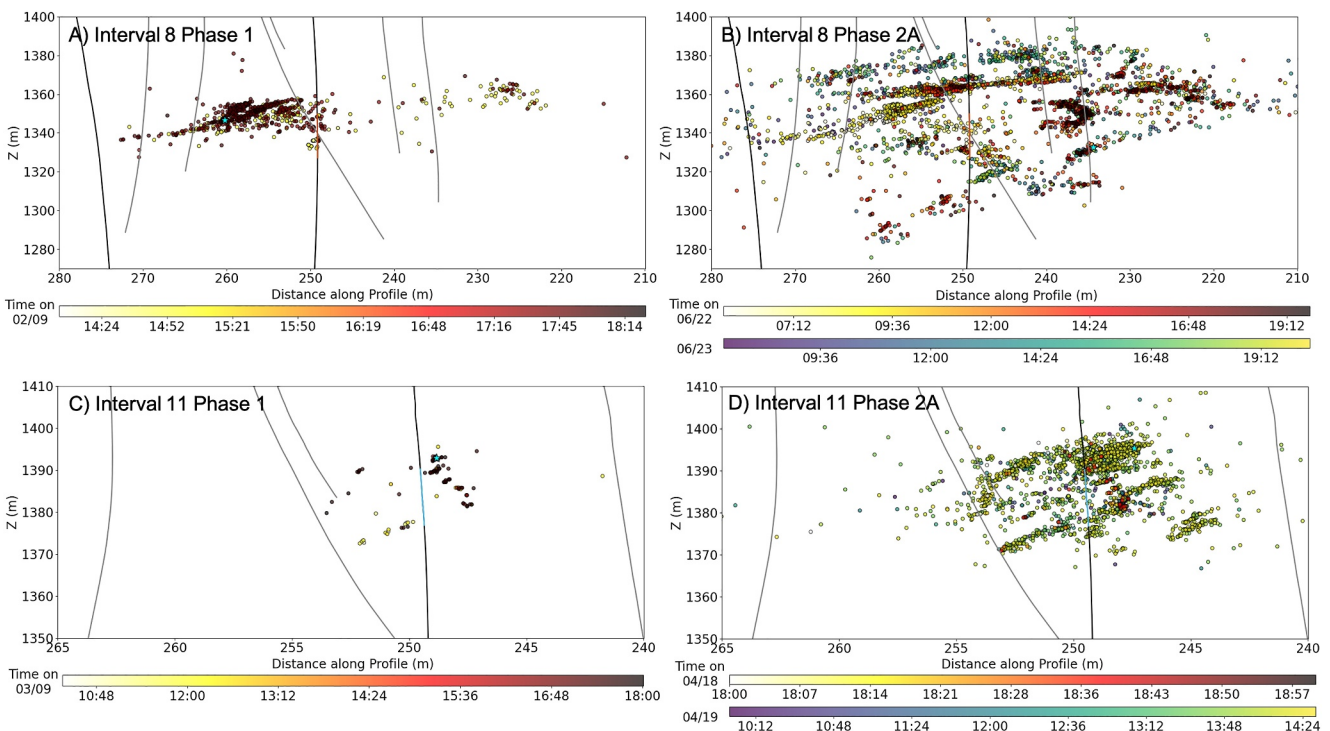


Figure 9. Spatio-temporal evolution of seismicity in selected intervals. (a) interval 8 phase 1, (b) interval 8 phase 2A, (c) interval 11 phase 1, (d) interval 11 phase 2A. For stimulations that lasted more than a day, we used two color-scales to differentiate the cycles. See Figure S5 in Supporting Information S1 for the profile location. Rotating 3D animations of the seismicity can be found in Movies S1–S4 of the Supporting Information S2.

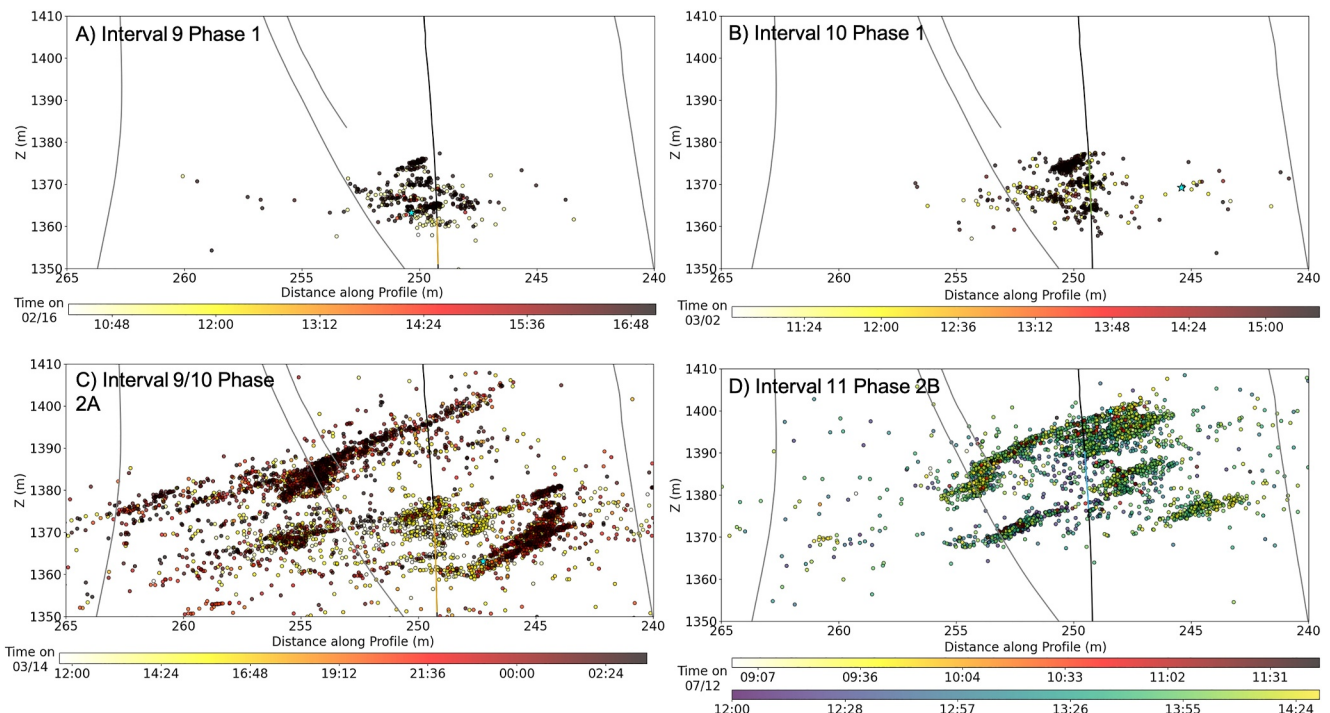


Figure 10. Spatio-temporal evolution of seismicity in selected intervals that showed hydraulic connectivity and activated the same structures. (a) interval 9 phase 1, (b) interval 10 phase 1, (c) intervals 9/10 phase 2A, (d) interval 11 phase 2B. See Figure S5 in Supporting Information S1 for the profile location. Rotating 3D animations of the seismicity can be found in Movies S5–S8 of the Supporting Information S2.

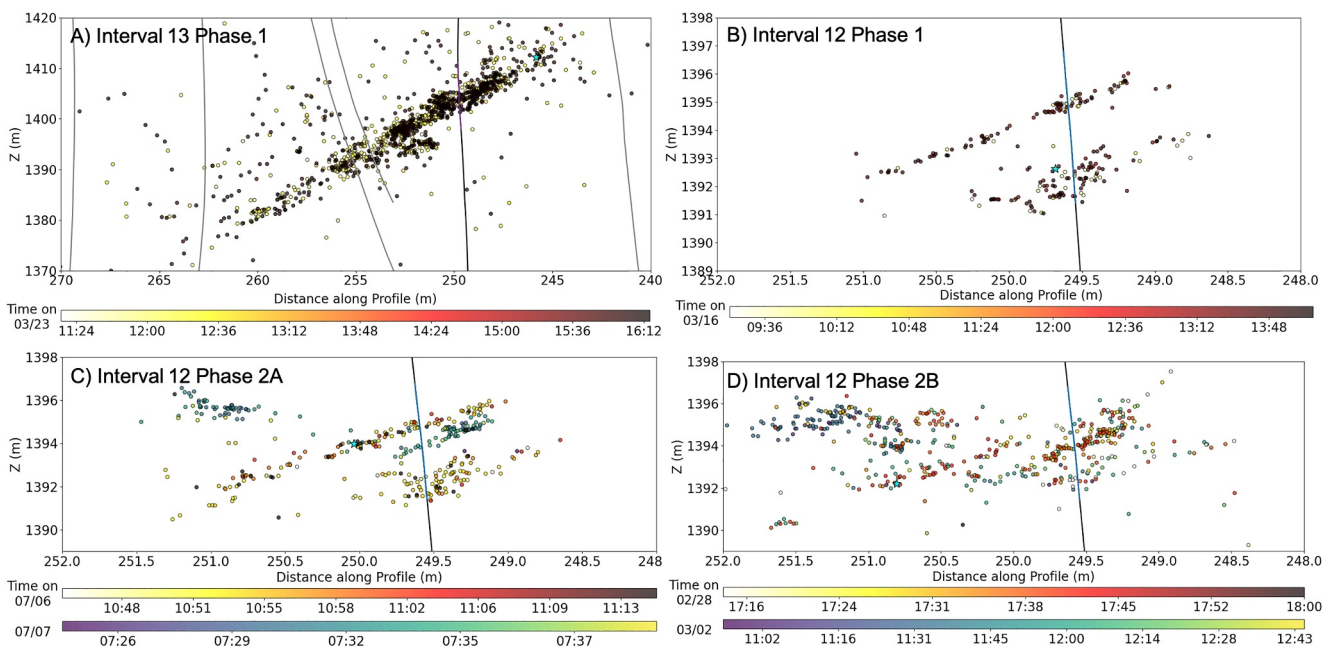


Figure 11. Spatio-temporal evolution of seismicity in selected intervals: (a) interval 13 phase 1, (b) interval 12 phase 1, (c) interval 12 phase 2A, (d) interval 12 phase 2B. For stimulations that lasted more than a day, we used two color-scales to differentiate the cycles. See Figure S5 in Supporting Information S1 for the profile location. Rotating 3D animations of the seismicity can be found in Movies S9–12 of the Supporting Information S3.

larger injection in the reservoir engineering phase, more than 12,000 seismic events were detected and the spatial extent of the seismic cloud exceeded 130 m. Several fractures were activated, covering different depth levels (Figure 9b). Seismicity moved from deeper to shallower sections of the volume, activating structures around interval 9 (Figure 9b). This second stimulation resulted in an additional almost four-fold increase in interval transmissivity.

Intervals 9 and 10 (phase 1: 832/922 detected events, 567/611 HQ events, phase 2A: 7,086 detected events, 6002 HQ events). The event locations for the phase 1 stimulations in both intervals were similar, indicating that the same fractures were stimulated (Figures 13a and 13b). The lateral extent of the seismicity cloud reached 30 m with no clear spatio-temporal evolution. The events highlighted two very small, but clearly differentiated planes in the upper part of interval 10. Seismicity in the lower part of interval 10 is more diffuse. During both phase 1 stimulations, no seismicity is observed around interval 9. The hydraulic data shows a strong hydraulic connection between interval 9 and 10 that was observed at about 11 MPa injection pressure during the first injection cycle in interval 9. During the reservoir engineering in phase 2A, the intervals were jointly stimulated. At the very beginning of this stimulation, the seismic events occurred again at two small fractures that were observed in phase 1 (Figure 12c). Then, seismicity was observed further upwards, activating larger fractures of about 50 m lateral

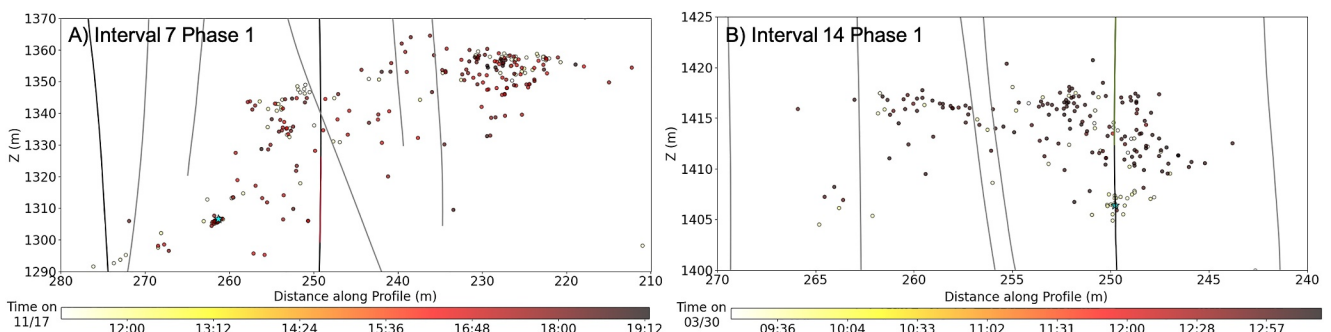


Figure 12. Spatio-temporal evolution of seismicity in selected intervals. (a) interval 7 phase 1, (b) interval 14 phase 1. See Figure S5 in Supporting Information S1 for the profile location. Rotating 3D animations of the seismicity can be found in Movies S13 and S14 of the Supporting Information S4.

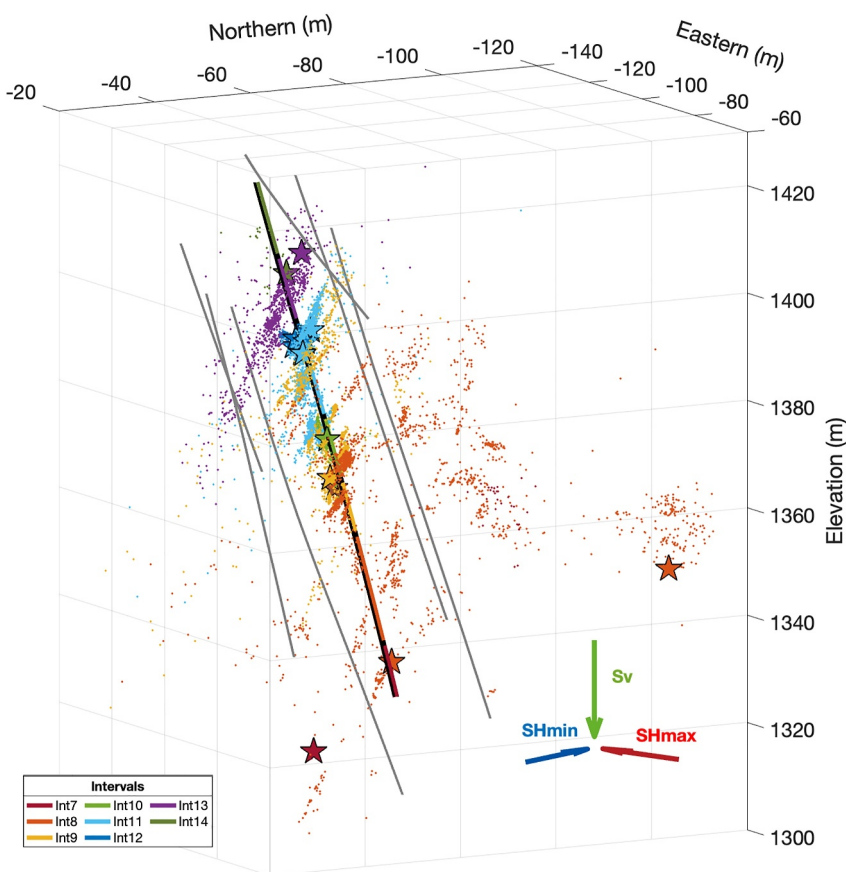


Figure 13. Overview of the HQ seismic events observed during stimulations in the various intervals. The largest events of each stimulation experiment are marked with a star.

extent, mostly parallel to the fracture planes stimulated in interval 8. Again, no seismicity was observed around interval 9, despite their reactivation during stimulations of interval 8.

Interval 11 (phase 1: 99 detected events, 98 HQ events, phase 2A: 4,087 detected events, 3848 HQ event, phase 2B: 5,310 detected events, 4615 HQ events). This interval showed rather low seismicity during the phase 1 stimulation (Figure 9c). When revisiting the interval during reservoir engineering (phase 2 A, B), the seismicity increased significantly to more than 4,000 and 5,000 events, respectively (Figures 9d and 10d). In the phase 2A stimulation, the seismicity initiated along two separate planes, at the middle and upper section of the interval. With time, the seismicity extended further outwards along the planes and additional parallel fractures were activated crossing into interval 12, and also in the lower part of the interval (Figure 9d). This trend was continued during the third stimulation (phase 2B), reaching 40 m of lateral extent (Figure 10d). Interestingly, it seems that extensions of two large fractures activated during the reservoir engineering in interval 11 had already been activated during the joint stimulation of interval 9 and 10 (Figure 10c).

Interval 12 (phase 1: 241 detected events, 233 HQ events, phase 2A: 500 detected events, 420 HQ events, phase 2B: 683 detected events, 599 HQ events). The lateral extent of seismicity was constrained to 10–20 m distance from the injection point, for all three stimulations (Figures 11b–11d). Nevertheless, the seismic cloud showed two clear clusters for phase 1 and three clusters for phase 2A, B. Additionally, the temporal evolution of the seismicity during stimulation 2A showed clearly that first the two fractures from phase 1 were activated, and at a later stage a third new fracture appeared (Figure 11c). During the third stimulation (phase 2B), we see seismicity in all three clusters during cycle 1 and cycle 2 (Figure 11d). This third structure coincides with the fracture crossing into interval 12 from the later interval 11 phase 2A stimulation. The transmissivity during the phase 2A stimulation increased approximately four-fold.

Interval 13 (phase 1: 5,146 detected events, 2417 HQ events). The majority of the 5,000 events detected during the stimulation showed a clear alignment with the main fracture zone in the volume with a lateral extent of about 40 m (Figure 11a). At the beginning, the seismicity occurred in the vicinity of the injection interval but quickly moved outwards along the fracture plane.

Interval 14 (phase 1: 460 detected events, 204 HQ events). Similar to the stimulation in interval 7, seismicity was diffusive with no clear alignment (Figure 12b). This shallowest interval is located at the edge of the dense seismic monitoring network.

Examples of the DTS, FBG, and DSS recordings for the Interval 9/10 Phase 2A stimulation are shown in Supporting Information S1 (Figures S6–S8).

In Figure 13, we plot the HQ catalog events for all stimulations. For displaying purposes, to have a clearer image of the activated structures, we removed the remaining scattered seismicity applying more restricting conditions. We plotted only the events with a minimum of 8 picks and more than 40 neighboring events. The search radius for neighboring events, lies within geophysically meaningful values; that is, the hypocentral separation between two events should be small compared to the event-station distance (Waldhauser, 2001). The first prominent observation is that most seismicity delineates fracture planes, with a predominant NE-SW direction of strike, dipping 70–80°, which coincides with the direction of known pre-existing fault structures obtained from the geological characterization (Bröker, Ma, Zhang, et al., 2024; Ma et al., 2022). The seismic events highlight decameter-long fractures, with interval 8 exceeding 130 m, yielding a clear impression of a hectometer-scale fractured reservoir. Several experiments showed (concentric) growth of seismicity (Phase 1 Intervals 8, 13; Phase 2 Intervals 8, 9/10, 12), while for other intervals (Phase 1 Intervals 7, 9, 10, 11, 12, 14) seismicity of subsequent cycles occurred at the same location, suggesting that the same fracture zones are reactivated (Figures 10 and 11). The spatial extent of the seismic clouds showed different behaviors for different intervals, ranging from 7 to 130 m (Table 3). With the exception of the stimulations in intervals 7 and 8, the largest event occurred in the vicinity of the injection points (Figure 13).

4.3. Seismicity Versus Injected Volume and Pressure

To better understand the relation between the induced seismicity (maximum magnitude, number of events, spatial extent) and the injection parameters (injection volume, pressure), we look at the data from different angles. We compare the maximum observed magnitude with the injected volume (Figure 14) and look at the number of detected events versus the cumulative injected volume (Figures 15a–15c) and the cumulative seismic energy (a proxy for active fracture area) versus the hydraulic energy (pressure × volume) (Figures 15d–15f). All key parameters can also be found in Tables 2 and 3. A summary of the observations from the individual intervals can be found in Supporting Information S1.

A hydraulic analysis (Gholizadeh Doonechaly, Bröker, Hertrich, Ma, et al., 2024) shows a major increase in transmissivity of intervals 8 (from 3.3×10^{-8} to $2.3 \times 10^{-7} \text{ m}^2/\text{s}$) and 14 (from 5.4×10^{-9} to $1.3 \times 10^{-7} \text{ m}^2/\text{s}$) after the phase 1 stimulation. Intervals 9, 10, 11 showed a strong hydraulic connection at elevated injection pressures, which is likely due to the presence of a conducting fracture in the direct vicinity of the borehole. Interval 13 was the most transmissive structure among the stimulated intervals. With >5,000 events (Table 3), we recorded most events in interval 13, followed by interval 8 (>2,000 events). The largest magnitudes per interval ranged from $M_w - 2.3$ (interval 13) to $M_w - 4.0$ (interval 14).

Most seismic events occurred during injection, only a handful were observed during shut-in (0%–12%, Table 3). Two remarkably large events with magnitudes $M_w - 2.0$ and -2.25 occurred in interval 8, phase 2A 5 hr after shut-in. These are the only events with $M > -3$ that occurred post-shut-in.

We compare the injected volume versus the maximum observed magnitude, using the approach from McGarr (2014) and Van Der Elst et al. (2016). McGarr (2014) proposes a model to estimate the maximum magnitude possible during injection activities. Assuming a *b*-value equal to one, the maximum scalar seismic moment released is simply the total injected volume (in m^3) multiplied by the shear modulus (in Pa). According to van Der Elst et al. (2016), the maximum magnitude is instead only what is statistically possible. So given an injected volume, one can estimate the total number of events expected above a certain magnitude of completeness by using the so-called seismogenic index (e.g., Shapiro et al., 2010). Given then a *b*-value and the total number of expected events, the maximum magnitude is simply the extrapolation of the frequency-magnitude distribution at

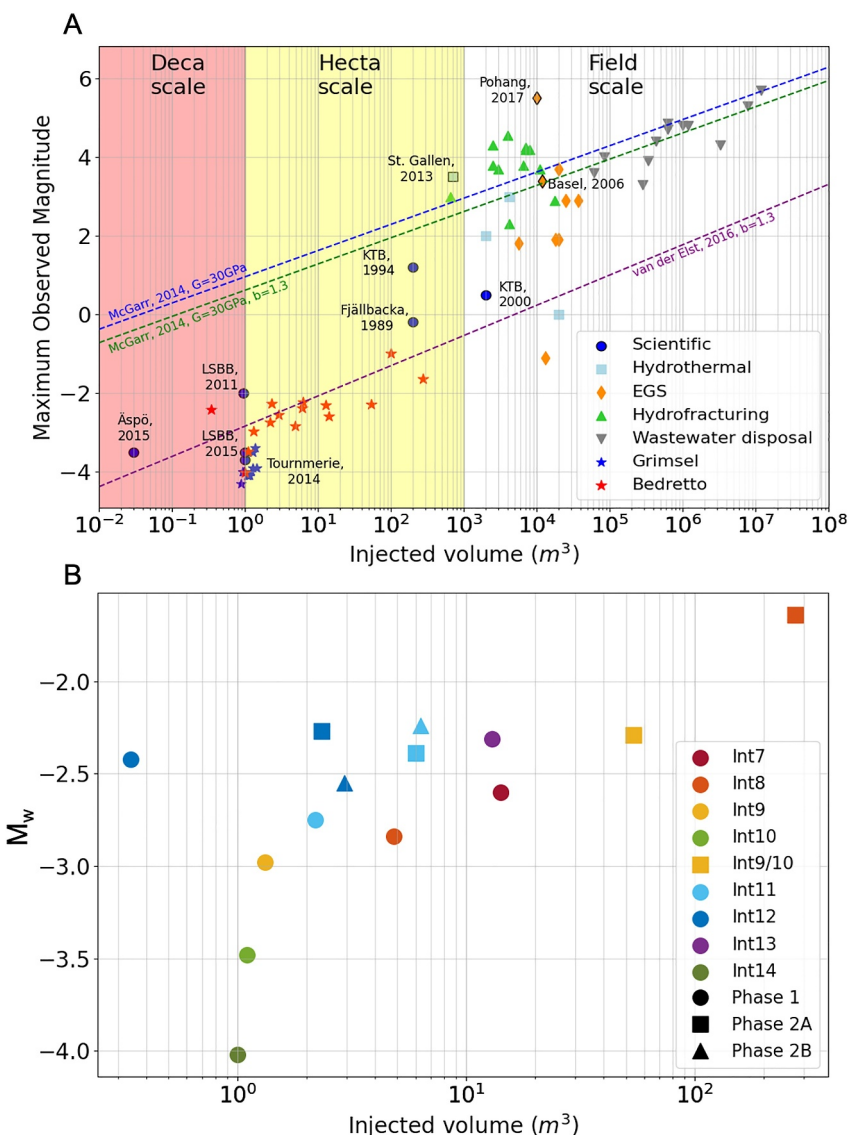


Figure 14. (a) Injected fluid volume versus maximum observed magnitude of seismicity at different scales, along with McGarr (2014) estimate of the maximum possible seismic magnitude with respect to the injected volume for a theoretical b -value of 1 (blue) and b -value of 1.3 (green), which is the average value from the Phase 2 stimulations. The figure also includes the maximum magnitude estimates by using the van der Elst et al. (2016) approach (violet), with the average b -value and an average seismogenic index of -3.7 . The magnitudes for the Grimsel experiments have been recomputed using Equation 1. (b) Zoom into the Bedretto stimulations highlighting changes of the observed magnitude with injection cycle.

the unity value. Our observations are about two magnitude scales below the postulated slope from McGarr (2014) for the maximum possible magnitude (Figure 14a). This is true both for the case of using a b -value 1 as well as a b -value of 1.3 (average of Phase 2 stimulation). However, when using the approach proposed by van der Elst et al. (2016), the recorded magnitude nicely aligns with the maximum magnitude based on the statistics of the large injections during the VALTER experiments (Phase 2, average b -value 1.3 and seismogenic index -3.7).

Most of the stimulations expose a near linear increase in maximum magnitude with injected volume (Figure 14b). Only the first two stimulations in interval 12, neighboring the main fault zone, show a substantially higher magnitude for low injection volumes, which is likely related to the hydraulic fracturing, that is, sudden pressure increases to break the fractures rather than the step-wise pressure/flowrate increases used in the other stimulations (Figures 14b and 15a). Variations in response can be observed for the different intervals. For instance, interval 9 and 14 in phase 1 have seen very similar injection volumes, but show a maximum magnitude

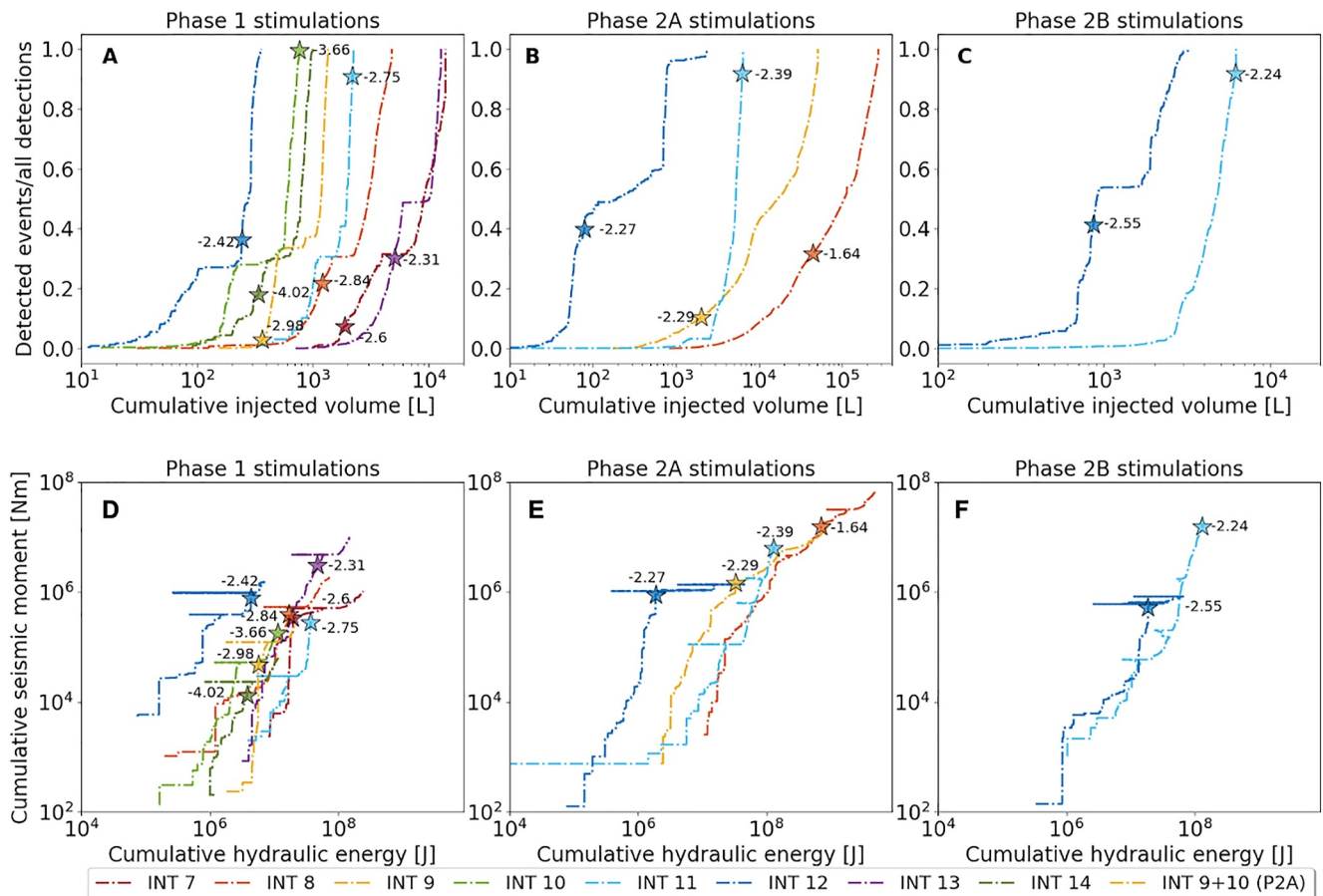


Figure 15. (a–c) Normalized cumulative fraction of detected events as a function of cumulative injected volume for the different phases. The maximum magnitude is marked by the star. (d–f) Cumulative seismic moment versus injected volume/cumulative seismic energy for the different phases. The largest events are marked with a star.

difference of one order of magnitude (Figure 14b). For the reservoir engineering stimulations in phase 2A and 2B, the intervals responded as expected from the characterization stimulations. For interval 8, 9/10, and 11 an increase in the maximum magnitude with higher injected volume was observed, whereas interval 12 did not show such a behavior. Here, the seismicity during all three stimulations was limited to a small area around the interval. Additionally, by the time the maximum magnitude occurred the flow rate was rather at a low level but the pressure increased fast for all interval 12 stimulations (Figure 15b).

Figures 15a–15c, show that seismicity started rapidly once a certain, interval dependent injection volume was reached. The threshold remained similar for repeated injections in phase 2A, B. For most intervals, the cumulative seismic moment reached its maximum with the largest magnitude and did not increase further with increased injection volumes (Figures 15d–15f). This effect is likely related to the limited pump capacity. Due to the high injectivity/transmissivity of interval 7 and 13, pressure and flow rate increased linearly.

4.4. Statistical Properties

We compute the Gutenberg-Richter b -value for all stimulations by fitting the observed seismicity rate and its evolution in dependence of the injection flow rate. Such a model, originally developed by Shapiro et al. (2007) and updated by Mignan et al. (2017), simulates the observed piecewise evolution of the seismicity rate λ during active injection and after shut-in:

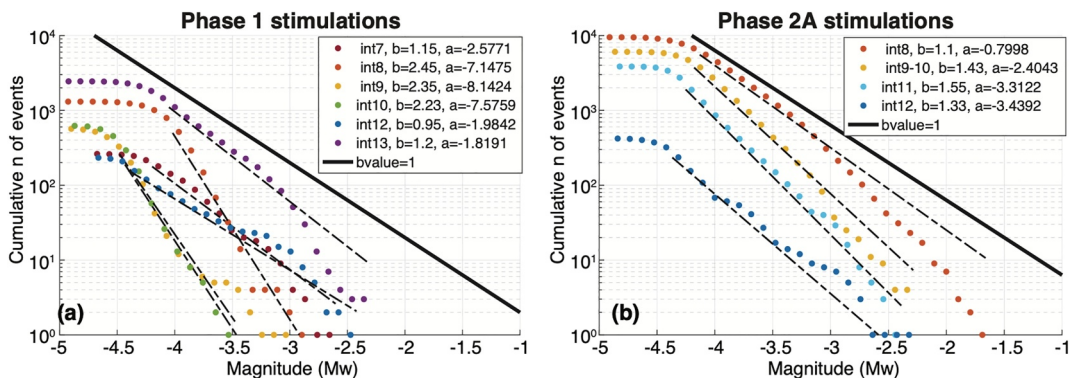


Figure 16. Frequency Magnitude distribution for Phase 1 (a) and Phase 2 (b). The Gutenberg-Richter b -value estimate was obtained through a Bayesian hierarchical model accounting for the injection flow rate and for the activation feedback parameters a_{fb} (seismogenic index).

$$\lambda(t, m > M_c) = \begin{cases} 10^{a_{fb}-bM_c} \dot{V}(t) & \text{if } t \leq t_s \\ 10^{a_{fb}-bM_c} \dot{V}(t_s) \exp\left(\frac{t-t_s}{T}\right) & \text{if } t > t_s \end{cases} \quad (2)$$

$V(t)$ is the injection flow rate as a function of time t and the model parameters a_{fb} , b , and τ are the activation factor or seismogenic index, the Gutenberg-Richter b -value and the mean relaxation time of the medium after the injection ends, respectively. M_c is the magnitude of completeness, estimated using maximum curvature method (Wiemer, 2000), and t_s is the shut-in time. For injection activities with multiple stages, the decay is considered only for the latest one. The model in Equation 2 assumes that the seismicity rate λ is modulated by the injected flow rate during the operational phase and that such rate decays exponentially as the injection stops. Following Broccardo et al. (2017), the model above can be fitted to the data through a Maximum Likelihood Estimation method or via a full Bayesian hierarchical approach, assuming that the seismicity rate λ can be well approximated by a Non-Homogeneous Poisson Process (NHPP). Figures 16a and 16b show the frequency-magnitude distribution and the model fit for several injections in Phase 1 and Phase 2. The estimated b -value is overall larger than 2 for all injections in the central region (Intervals 8, 9, 10), while it is close to 1 for larger volume injections in Phase 1 (Intervals 7 and 13) and Interval 12. For Phase 1, the fit is not shown for Interval 11 and 14, for which a very small number of events were detected with magnitudes above completeness (Table 3). In Phase 2 the estimated b -value is smaller on average, ranging from a value of 1.1 (Interval 8) to 1.55 (Interval 11).

Figures 17a and 17b show that the confidence intervals (5th to 95th percentile) for both, b -values and activation feedback, is quite large for all injections in Phase 1, except for Interval 13, where a large number of events was

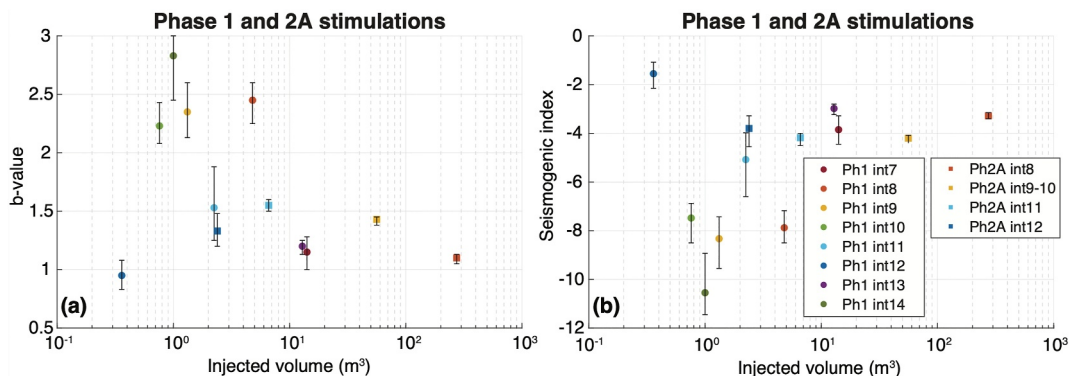


Figure 17. Estimated Gutenberg-Richter b -values and activation feedback (seismogenic index) with confidence interval (5th–95th percentile) for all injections in Phase 1 and Phase 2.

detected. All injections in Phase 2, in particular the ones with large volumes, show a very constrained estimate of the b -value and the activation feedback (seismogenic index), with the average b -value between 1.1 and 1.5 and a seismogenic index around a value of -4.

5. Discussion

5.1. Network Sensitivity

With a covered frequency range of 50 Hz–100 kHz, the ultra-high frequency AE network is optimal for the analysis of pico- to microseismic events with $M < -2$ that have a dominant frequency content above 1 kHz. For source analysis of events $M > -3$ the recordings of the VALTER geophones and broadband stations should be taken into account in addition, which cover the frequency range 0.08 Hz–1 kHz. The ultra-high frequency network is limited by the fast decay of high-frequency signals in the attenuating rock mass, as shown in Figures 5b and 5c. While we succeed in creating high-resolution monitoring in the rock volume adjacent to the injection borehole and directly affected by the stimulation, we are not able to monitor the same small magnitudes in more distant regions, where picoseismicity was potentially also directly or indirectly triggered by the stimulation.

Thanks to collocated ACC and AE sensors, AE sensors could be calibrated in this study in situ, and adjusted moment magnitudes could be implemented into the seismic catalog. Nonetheless, the remaining limitation in AE sensor calibration to 20 kHz leaves room for uncertainties. To have a comparative assessment of the network sensitivity, we recomputed the magnitudes from the decameter injection experiments in Grimsel (Villiger et al., 2020) using Equation 1. In Grimsel, the network consisted of clamped AE sensors GMuG-Ma-Blw-7-70 in open decameter boreholes and AE sensors GMuG-Ma-Bls-7-70 along the tunnel wall at distances of at least 15 m from the events (Jalali et al., 2018). For distances larger than 15 m, we observe an improved sensitivity of the VALTER network of about 0.3 magnitude points. The improvement can be attributed, besides small differences in seismic damping Q , to the VALTER AE sensors, which have a smaller bandwidth than the sensors used in Grimsel, but an increased sensitivity in the frequency range in the lower kHz range. In the very near-field (< 15 m), the sensitivity of the Grimsel network seems larger due to the more broadband AE sensor used that is better suited for the recording of frequencies above 50 kHz. The sensitivity then rapidly decays with distance, causing a break in the slope. This observation highlights our current limits in the magnitude estimation methods, as well as limitations in the AE sensor calibration. Only dedicated calibration experiments of AE sensors focusing on the < 100 kHz range can help to answer whether this observation hints at an intrinsic breakdown of failure in the scaling laws of the seismic events, or is simply related to the magnitude estimation methods.

5.2. Illumination of a Fracture Network

The studied rock volume is characterized by sub-parallel continuous fractures, a feature observed both in surface outcrops (Ceccato et al., 2024) and within the tunnel (Bröker, Ma, Zhang, et al., 2024; Rast et al., 2022). The dominating strike direction of the largest structures is NE-SW to ENE-WSW. This pervasive geometry is consistent with the orientation of the seismogenic features resulting from the distribution of recorded events (Figure 13). The brittle fault zones described in Phase IV of Ceccato et al. (2024) share the same NE-SW to ENE-WSW orientation as these subparallel fractures. These zones correspond to brittle shear zones organized into clusters, with lateral extents reaching several hundred meters and spacings of tens of meters along the strike direction. A detailed correlation of mapped fracture planes from geological characterization based on logging data and cores with the seismogenic features highlighted in this work is beyond the scope of this paper and will be addressed in future studies.

In terms of slip tendency, steeply dipping (60–70°) and ENE-WSW striking fractures are optimally oriented for shear reactivation, if we assume a far field SHmax direction of around N112°E (Bröker, Ma, Zhang, et al., 2024). However, studies of borehole breakouts along the stimulation and monitoring boreholes showed strong stress field rotations and variability (Zhang et al., 2023) that are difficult to resolve throughout the stimulated volume. Therefore, the slip tendency of fractures varies spatially, especially around the large fault zone intersected in interval 13.

A common feature of most stimulations is that in most intervals (except in interval 13) several transmissive structures were stimulated, and not only a single most transmissive fracture. In deep reservoir stimulation it is often interpreted that only very few fractures were reactivated during large open-hole stimulation (e.g., Baisch

et al., 2006; Evans, Genter, & Sausse, 2005; Evans, Moriya, et al., 2005; Kraft & Deichmann, 2014). In our case, through the simultaneous stimulation of several fractures in each interval, a 3D network of fractures reactivated at least in the decameters around the boreholes as made visible from the high-resolution seismicity clouds. This is not only the case for the more extended stimulation in Interval 8 and 9 + 10 during phase 2 but also for the smaller-volume stimulations. Thus, the data set allows now to analyze the influence of the small-scale fracture network on the stimulation, which might be a poorly understood parameter in full-scale experiments. The interval-specific stimulated 3D fracture networks in combination with the capability of selectively stimulating individual intervals (i.e., zonal isolation) showed that an extended 3D reservoir can be developed, giving confidence that the zonal isolation techniques may lead to improved reservoir geometry on the full-scale.

Throughout all stimulations, seismicity occurred in confined patches, that is, concentration of seismicity with seismically “quiet” zones around. Similar patterns have been observed during the stimulation experiments at the Grimsel Test Site (Villiger et al., 2020), where they have been interpreted as asperities bounding flow channels. It was argued that this conceptual model agrees with those proposed by Rutledge et al. (2004), Evans, Genter, and Sausse (2005), and Evans, Moriya, et al. (2005). The inferred strongly channelized flow characteristics imply that, although a 3D network was stimulated, the flow may be strongly heterogeneous, which has implications for the operation of full-scale operations. Further work toward integrating strain and pressure observations in this well-instrumented rock volume will give further insights into the flow field during stimulations and allow deriving implications for geothermal projects in crystalline rock.

Apart from these similarities in the overall spatial seismicity characteristics, the details of the seismicity cloud evolution are distinct for each interval. For instance, the seismicity around interval 13 remains confined to the dominant shear zone, while the stimulations of interval 9, 10 and 11 connect to the same fracture network and produce seismicity extending over various depths levels.

5.3. Variability of Seismic Responses

The variability in the spatio-temporal evolution of seismicity is also reflected in other seismicity characteristics as seen in Figure 18. In Figure 18, we visually summarize some of the stimulations' key parameters from Tables 2 and 3, such as injected volume, number of detected events, M_{\max} , a_{fb} and b -values, seismic activation pressure, interval reactivation pressure and the extent of the seismic cloud. The reactivation pressure P_R is computed from pressure-flow rate plots (Bröker, Ma, Doonechaly, et al., 2024). If available, we here differentiate between the pressures needed in the individual cycles (C1, C2) of the injection protocol. The seismic reactivation pressure, P_S , is the average pressure prevailing during the occurrence of the first 5% of seismic events.

The number of seismic events ($>M_c$) ranges from <100 to $>5,000$. While this variability may partially be explained by the varying injection volumes, the a_{fb} and b -value gives largely volume-independent information on seismic productivity. We observe a large scatter in b - (0.95–2.83) and a_{fb} - (-1.55 to -10.55) values that seems to reduce for larger injected volumes ($>7 \text{ m}^3$) with b -values around 1.35 ± -0.2 and a_{fb} around -3.9 ± -0.2 . The large scatter might correspond to the significant variations of the hydrological and mechanical properties already observed during the rock volume characterization (Ma et al., 2022). In Grimsel, where the maximal injected volume reached only 1.45 m^3 , a similarly large scatter of the statistical properties was observed, with values fluctuating in the same range (b : 1.0 to 2.6, a_{fb} : -2.4 to -9.0). However, increased seismic responses (low b -values and high a_{fb} values) could be attributed to stimulations performed in highly conductive brittle–ductile shear zones (Villiger et al., 2020). A physical explanation for the large variability could be that with smaller injected volumes, we sample a smaller rock volume so that local fracture properties and stress conditions govern seismicity. For larger injected volumes, larger rock volumes are accessed and smear the local properties. The few experiments with volume $>10 \text{ m}^3$ (Figure 17) may support that injections at larger volume led to a more similar seismic response in terms of magnitude statistics. Evidently the larger volume injections in interval 8 and 9 + 10 (and also interval 11) during phase 2 accessed a similar fracture network making a similar seismic response conceivable. A second order effect could also arise from the different injection pattern between Phase 1 (small injections) and Phase 2 (large injections), however a full analysis of the spatio-temporal evolution is necessary to fully evaluate these effects.

During the smaller volume injection in phase 1, we observe that the seismic response is “most intense” (i.e., highest a_{fb} -value, lowest b -value) in the transmissive interval 7 as well as in interval 13 (including interval 12, which may have connected with shear zone of interval 13). It is noteworthy (although not able to stand up to a

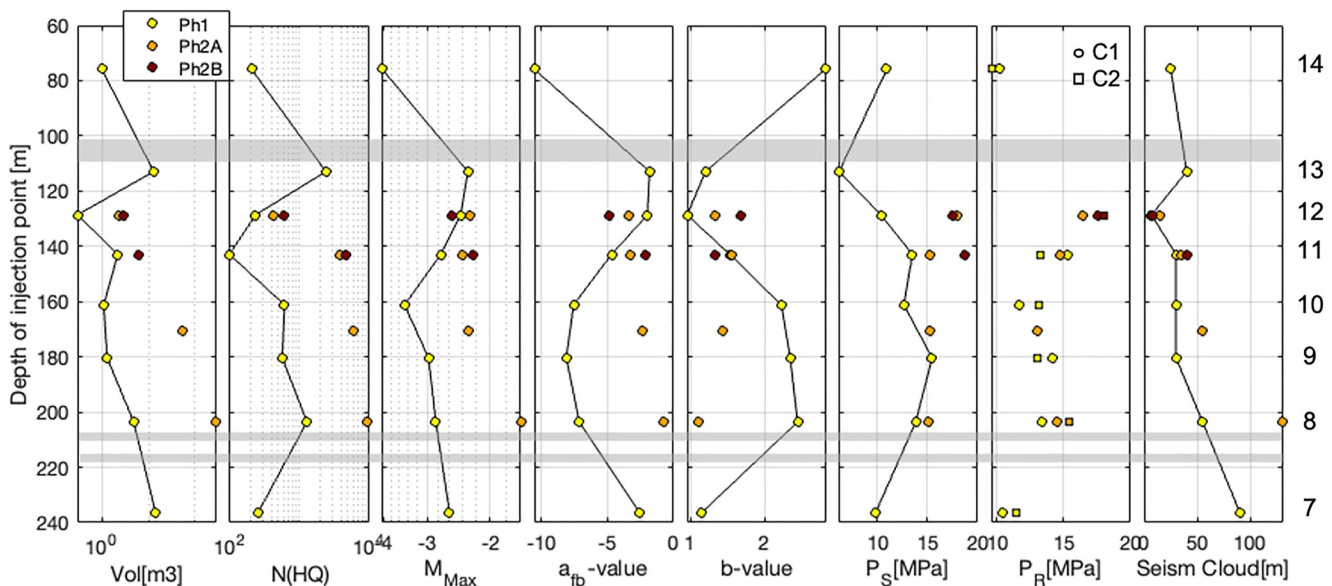


Figure 18. Visual representation of key observables from the stimulation intervals given by their injection point depth from Tables 1 and 2 and color-coded by stimulation phase. From left to right, we plot the injection volume, the number of HQ events, the Maximum Magnitude, the a_{fb} , and b value, the seismicity activation pressure P_s (first 5% of seismicity), the reactivation pressure P_R and the lateral extent of the seismic cloud. The gray zones mark the main shear zone in interval 13 and the two non-filled fractures in interval 8. The points belonging to Phase 1 (Ph1) are connected to highlight the hyperbola-like pattern with distance from the fault zones.

statistical test) that the seismic reactivation pressure P_s seems to roughly follow a similar pattern: low reactivation pressure is associated with a more intense seismic response at interval 7 and 13, which may be interpreted that both reflect more critically stressed conditions around these zones. At the same time, these intervals have been the most transmissive ones. Looking only at the key observables from the characterization stimulations (Phase 1), we observe a pattern like a hyperbola, seemingly sandwiched between the main shear zone in interval 13 and the two unfilled fractures in interval 8. We speculate that the diversity we see in seismic response correlates first order to the distance to the dominant shear zones in the volume.

Variability is also reflected in the number of post-shut-in events. While seismicity correlates dominantly with active stimulation phases (80%–100%) or occurs within <5 hr after shut-in (Table 3, Figures S1–S3 in Supporting Information S1), interval 8, Phase 2, saw two remarkably large events with magnitudes $M_w = 2.0$ and -2.25 5 hr after shut-in. A similarly low number of post-shut-in events was observed in other decameter stimulation experiments (Boese et al., 2022; Kwiatek et al., 2018; Villiger et al., 2020). The percentage of post-shut-in events to total events tends to be lower than in many full-scale geothermal projects that have seen up 30% event occurring after shut-in (Basel: Catalli et al., 2013, Mukuhira et al., 2017; Pohang: Yeo et al., 2020; Soultz-sous-forêt, Evans, Genter, & Sausse, 2005; Evans, Moriya, et al., 2005). The difference to full scale observations might be site dependent, or might demonstrate the limitations in process understanding when studying the ongoing processes on a smaller scale.

Additionally to the geometric argument, also a comparison of the reactivation pressures (Figure 18, PQ and the seismic activation pressure) with the estimated stress field, indicate hydraulic shearing as the dominant process for the stimulations in the Geothermal Testbed.

5.4. Implications for Upscaling

Activities at the BULGG are part of the strategy to investigate hydraulic stimulation and induced seismicity processes at different scales, and thus lie half-way between the decameter-scale of experiments at the Grimsel Test Site (Villiger et al., 2020), Aspö (Kwiatek et al., 2018), STIMTEC (Boese et al., 2022), EGS collab (Fu et al., 2021), on the one hand, and the full-scale like the multi-stage stimulations done by Norbeck and Latimer (2023) and the planned EGS project in Haute-Sorne, Switzerland (Meier et al., 2015), on the other hand. While the decameter-scale stimulations at the Grimsel Test Site were at roughly 1 m^3 scale, the characterization

stimulations of phase 1 in BULGG range from 0.3 to 14 m³. At this scale, the enormous variability in seismicity characteristics in terms of a_{fb} - and b -values (Figure 17) as well as the trailing effect is comparable to what has been found at Grimsel Test Site. The large variability, likely associated with local geological and geomechanical conditions, has far-reaching implications for the use of small-volume injections to calibrate seismic hazard forecasts. For instance, intervals 14 and 13, despite lying close to each other, show very distinct seismic responses, which renders the predictability of the seismic response from one interval to the next questionable. Note that small injection volumes produce fewer seismic events and hence less stable estimates of b and a_{fb} , which is reflected in the larger errors of the b and a_{fb} values (Figure 17). In contrast, the more extended stimulations of phase 2, with volumes ranging from 5 to 274 m³, show less variability compared to the phase 1 stimulations with b -values ranging from 1.1 to 1.68 and a_{fb} -values from -5.3 to -2.9. The reduction in variability may be related to the large rock volume that is accessed with larger volume thus averaging the more local-scale response to one that is more representative of the rock volume. Thus, injections with >10 m³ may be necessary to obtain seismicity characteristics that allow upscaling of seismic hazard to neighboring volumes or larger injection volumes. However, additional observations are necessary to conclude whether a minimum injected volume is necessary to converge to stable a and b values.

5.5. Implications for Reservoir Development

While the goal of decameter-scale experiments has so far been focused on process understanding of hydraulic stimulation and induced seismicity, the experimental approach at the BULGG aimed at testing reservoir development technologies, namely zonal isolation and multistage stimulation as key technology developments for EGS. Zonal isolation techniques may include cemented casing perforated with shot-guns (Norbeck & Latimer, 2023) or micro-drilling, or sliding-sleeves accessing to packed-off intervals, as tested in ST1. Generally, advantages of zonal isolation are (a) a more extended and three-dimensional volume can be stimulated, (b) because stimulation of each interval tends to be smaller in volume and may individually be controlled in terms of seismic hazard (e.g., ATLS), (c) disadvantageous intervals in terms of suboptimal flow characteristics (too high transmissivity and connectivity leading to short-cuts) and/or seismic response can be avoided in favor of more advantageous intervals.

The tested volume at BULGG has ideal conditions to assess some of these aspects; with the different compartments with distinct flow characteristics as well as a large transmissive shear zone fault (Interval 13) that can easily be reactivated and is potentially seismogenic, the rock volume can be seen as an analog to conditions that may be found in deep reservoir (e.g., in the crystalline rock targeted in Haute-Sorne, Switzerland). Thus, our seismicity data sets can provide insights into the impact of zonal isolation with sliding-sleeves on induced seismicity and reservoir development. We observed that indeed an extended 3D fracture network has been stimulated. A hypothetical massive open-hole stimulation instead of the multi-stage stimulation would have likely led to the stimulation of the most transmissive intervals (e.g., intervals 7, 13) alone. Consequently leading to very limited transmissivity increase and restricted accessed reservoir volume. However, we also observe that some intervals may connect to the same rock volume (e.g., intervals 8, 9, 10). Although the individual stimulations of each of these intervals showed slightly different spatial characteristics, it is questionable if stimulating all three intervals at the same time would have led to more much different spatial characteristics.

Future work may also compare the sliding-sleeves techniques with zonal isolation with cemented boreholes. Although the fact that several transmissive fractures per interval were reactivated is advantageous regarding reservoir and flow geometry, even more targeted and controllable stimulations may be achieved from perforated cemented boreholes. After stimulation, some intervals showed decreased or unchanged transmissivity. This variability underscores the influence of geological factors and stimulation methods on reservoir performance in Enhanced Geothermal Systems, highlighting the need for further study to optimize future developments.

6. Conclusions

6.1. Observations

With the hectometer-scale hydraulic stimulation experiments in the BedrettoLab, we anticipated to fill the gap between decameter experiments in underground laboratories and the km scale of engineering projects. We succeeded in stimulating a complex 100 m + fracture network imaged by pico-seismic events. Overall, more than 40,500 seismic events were located with magnitudes down to $M_w = 5$. The maximum observed magnitude was

$M_w = 1.64$ during the stimulation in interval 8, while injecting with the largest volumes. Besides the triggered seismic catalogs, continuous waveform data at 200 kHz sampling rate was recorded for all stimulations. We started the seismic analysis by comparing the different injection intervals.

The volume impacted by the stimulations in different intervals differs significantly with a lateral extent from a few meters to more than 150 m. Most intervals activated multiple fractures with seismicity typically propagating upwards toward more permeable, shallow depth (intervals 8, 9, 10, 11). Seismicity occurs on parallel dipping planes that are consistent with the stress field and seem to a large extent associated with preexisting open fractures.

The experiments confirm the diversity in seismic behavior independent of the injection protocol. Some intervals showed rapidly increasing seismicity that is spatially restricted to the volume in direct vicinity of the injection point (e.g., interval 12, phase 1), while others have seismicity extending as far as 150 m away from the injection point (e.g. interval 8, phase 2). The reactivation pressures hint at hydraulic shearing as the dominant process for the stimulations in the Geothermal Testbed, since the elastic fracture opening appears to be mostly aseismic (Bröker, Ma, Doonechaly, et al., 2024; Bröker et al., 2023).

We see substantial variability in seismogenic index, b -value, number and magnitude of seismic events. The scatter in b -value ranges from 0.95 to 2.83 and in a_{fb} from -1.55 to -10.55 . The values seem to reduce for larger injected volumes ($>7 \text{ m}^3$) with b -values around $1.3 + -0.2$ and a_{fb} around $-3.7 + -0.2$. The magnitude distributions of seismicity show so far no distinct deviation from typical Gutenberg-Richter distribution. While we evaluated only the first-order effect, a full analysis of clustering would potentially highlight the spatio-temporal pattern of the statistical properties and would help shed light on the role of injection strategy on seismicity.

6.2. Lessons Learned for Upscaling

Since seismicity occurs mainly on preexisting fractures, activating dominantly the ones well-oriented within the stress field for hydroshearing, a hydromechanical characterization based on the classification of filled/non-filled fractures at the borehole wall from initial borehole logging and core analysis is essential for a prior understanding of the seismic potential. In the presence of several boreholes, the volumetric extent of the mapped fractures can already give us an understanding of the optimally aligned surfaces that are likely to be activated.

Multistage stimulations prove to be very important to effectively increase transmissivity. Hydraulic stimulations with small injection volume ($>10 \text{ m}^3$) helps identify transmissive structures and characterize the seismic response that can be used for seismic hazard estimations prior to large-scale stimulations. Even though the granite appeared relatively homogeneous in the Geothermal Testbed volume (e.g., Lützenkirchen & Loew, 2011), fractures and shear zones that crosscut the granite create substantial localized inhomogeneities that are reflected in a large variability of the seismic response and possibility to increase transmissivity.

6.3. Outlook

We have the opportunity to analyze the seismic data jointly with a multitude of other geophysical observables, such as strain and pressure, to allow more insights into the correlation of slow fracture opening and aseismic deformation processes. In future studies, the existence of these multi-disciplinary observations will allow us to put more constraints on the processes responsible for the diversity observed in seismicity.

Understanding the reasons for the variability in seismicity and the influence of geological features, stress field, and pore pressure on hectometer scale would be an important step toward understanding the variability of induced seismicity and improving the controllability of full-scale operational sites. It will be interesting to investigate further the role of shear zones and the spatial extent of their influence.

Since seismicity is the only data set able to cover the full rock volume and even address features on cm-scale, in the future, more advanced full waveform analysis of the picoseismic events will give a more complete picture on the rock volume with regard to stress, fracture composition and fracture response to stimulation. Accordingly, studies are currently in progress using both active transmission signals of the ultrasonic transmitters and the picoseismic events to gain in-depth knowledge. Methods like moment tensor inversion for fault plane orientations, stress inversion for spatial-temporal evolution of stress conditions, coda-wave inversion will be applied.

While more detailed source properties are yet to be computed, we already see that the source sizes are on the dm to cm-scale. Seismic events with source sizes of tens of meters were not recorded. Seismicity is therefore not able to account for the dimension of the fracture network observed and we can conclude that the fracture network was pre-existing as imaged by picoseismic events occurring on or in the vicinity of these pre-existing faults. To which extent aseismic processes interact with the fault system is unknown at the moment, but might be approachable in future studies by a joint analysis with the geomechanical data collected in VALTER.

Data Availability Statement

The seismic catalogs were produced using the DugSeis software package (Rosskopf et al., 2024d) that is open source and freely available on GitHub. The software release associated with this paper can be found on zenodo under Rosskopf et al. (2024a). The seismic catalogs are accessible in the ETH research collection under Rosskopf et al. (2024c).

Acknowledgments

In the “Bedretto Underground Laboratory for Geosciences and Geoenergies,” ETH Zurich studies in close collaboration with national and international partners techniques and procedures for a safe, efficient, and sustainable use of geothermal heat and questions related to earthquake physics. The BedrettoLab is financed by the Werner Siemens Foundation, ETH Zürich and the Swiss National Science Foundation. The research in this publication was conducted within the project VALTER and has received additional funding by the Swiss Federal Office of Energy (SFOE). The BedrettoLab would like to thank Matterhorn Gotthard Infrastructure for providing access to the tunnel. The PhD student Martina Rosskopf has been supported by the SNF Multi PhD project 200021_192151. Instrument purchase has been supported by the SNF Requin 206021_189632. A special thanks goes to the BedrettoLabTeam to make the stimulations possible and to Rebecca Hochreutener for keeping all administrative aspects off our shoulders. This paper is BULGG publication [BPN]. We are very grateful to the two reviewers Jake Walter and Grzegorz Kwiatek, as well as the associate editor Alexandre Schubnel, who provided excellent reviews that allowed us to much better highlight the scientific relevance of our experiments and findings.

References

- Achziger-Zupančič, P., Ceccato, A., Zappone, A. S., Pozzi, G., Shakas, A., Amann, F., et al. (2024). Selection and characterization of the target fault for fluid-induced activation and earthquake rupture experiments. *Solid Earth*, 15(8), 1087–1112. <https://doi.org/10.5194/se-15-1087-2024>
- Adelinet, M., Dorbath, C., Cal’o, M., Dorbath, L., & Le Ravalec, M. (2016). Crack features and shear-wave splitting associated with fracture extension during hydraulic stimulation of the geothermal reservoir in Soultz-sous-Forêts. *Oil & Gas Science and Technology—Revue d’IFP Energies Nouvelles*, 71(3), 39. <https://doi.org/10.2516/ogst/2015023>
- Allis, R., Moore, J., Davatzes, N., Gwynn, M., Hardwick, C., Kirby, S., et al. (2016). EGS concept testing and development at the Milford, Utah FORGE site. In *Proceedings 41st workshop on geothermal reservoir engineering*. Stanford University. SGP-TR-209.
- Amann, F., Gischig, V., Evans, K., Doetsch, J., Jalali, R., Valley, B., et al. (2018). The seismo-hydromechanical behavior during deep geothermal reservoir stimulations: Open questions tackled in a decameter-scale in situ stimulation experiment. *Solid Earth*, 9(1), 115–137. <https://doi.org/10.5194/se-9-115-2018>
- Bagagli, M. (2021). *Aurempickers*. Zenodo. <https://doi.org/10.5281/zenodo.5459631>
- Baisch, S., Weidler, R., Vörös, R., Wyborn, D., & de Graaf, L. (2006). Induced seismicity during the stimulation of a geothermal HFR reservoir in the Cooper Basin, Australia. *Bulletin of the Seismological Society of America*, 96(6), 2242–2256. <https://doi.org/10.1785/0120050255>
- Barbier, E. (2002). Geothermal energy technology and current status: An overview. *Renewable and Sustainable Energy Reviews*, 6(1–2), 3–65. [https://doi.org/10.1016/s1364-0321\(02\)00002-3](https://doi.org/10.1016/s1364-0321(02)00002-3)
- Boatwright, J. (1978). Detailed spectral analysis of two small New York State earthquakes. *Bulletin of the Seismological Society of America*, 68(4), 1117–1131.
- Boese, C. M., Kwiatek, G., Fischer, T., Plenkers, K., Starke, J., Blümle, F., et al. (2022). Seismic monitoring of the STIMTEC hydraulic stimulation experiment in anisotropic metamorphic gneiss. *Solid Earth*, 13(2), 323–346. <https://doi.org/10.5194/se-13-323-2022>
- Broccardo, M., Mignan, A., Grigoli, F., Karvounis, D., Rinaldi, A. P., Danciu, L., et al. (2020). Induced seismicity risk analysis of the hydraulic stimulation of a geothermal well on Geldinganes, Iceland. *Natural Hazards and Earth System Sciences*, 20(6), 1573–1593. <https://doi.org/10.5194/nhess-20-1573-2020>
- Broccardo, M., Mignan, A., Wiemer, S., Stojadinovic, B., & Giardini, D. (2017). Hierarchical Bayesian modeling of fluid-induced seismicity. *Geophysical Research Letters*, 44(22), 11–357. <https://doi.org/10.1002/2017GL075251>
- Bröker, K., & Ma, X. (2022). Estimating the least principal stress in a granitic rock mass: Systematic mini-fract tests and elaborated pressure transient analysis. *Rock Mechanics and Rock Engineering*, 55(4), 1931–1954. <https://doi.org/10.1007/s00603-021-02743-1>
- Bröker, K., Ma, X., Gholizadeh Doonechalay, N., Obermann, A., Rosskopf, M., Rinaldi, A. P., et al. (2024). Hydromechanical characterization of a fractured crystalline rock during multistage hydraulic stimulations at the BedrettoLab. *Geothermics*, 124. <https://doi.org/10.1016/j.geothermics.2024.103126>
- Bröker, K., Ma, X., Gholizadeh Doonechalay, N., Hertrich, M., Hansruedi, M., Giardini, D., et al. (2023). Hydro-geomechanical observations during multistage hydraulic stimulation at the Bedretto underground laboratory, Switzerland. In *ARMA US rock mechanics/geomechanics symposium*. ARMA. <https://doi.org/10.56952/ARMA-2023-0472>
- Bröker, K., Ma, X., Zhang, S., Gholizadeh Doonechalay, N., Hertrich, M., Klee, G., et al. (2024). Constraining the stress field and its variability at the BedrettoLab: Elaborated hydraulic fracture trace analysis. *International Journal of Rock Mechanics and Mining Sciences*, 178, 105739. <https://doi.org/10.1016/j.ijrmms.2024.105739>
- Bussien, D., Bussy, F., Masson, H., Magna, T., & Rodionov, N. (2008). Variscan lamprophyres in the Lower Penninic domain (Central Alps): Age and tectonic significance. *Bulletin de la Société Géologique de France*, 179(4), 369–381. <https://doi.org/10.2113/gssgbull.179.4.369>
- Castilla, R., Serbeto, F., Christe, F., Meier, P., Bethmann, F., Alcolea, A., et al. (2022). Data integration and model updating in a multi-stage stimulation in the Bedretto Lab, Switzerland. In *ARMA US rock mechanics/geomechanics symposium* (p. ARMA-2022). ARMA.
- Catalli, F., Meier, M. A., & Wiemer, S. (2013). The role of Coulomb stress changes for injection-induced seismicity: The Basel enhanced geothermal system. *Geophysical Research Letters*, 40(1), 72–77. <https://doi.org/10.1029/2012gl054147>
- Ceccato, A., Behr, W. M., Zappone, A. S., Tavazzani, L., & Giuliani, A. (2024). Structural evolution, exhumation rates, and rheology of the European crust during Alpine collision: Constraints from the Rotondo granite—Gotthard nappe. *Tectonics*, 43(6), e2023TC008219. <https://doi.org/10.1029/2023tc008219>
- Ceccato, A., & Pennacchioni, G. (2018). Structural evolution of the Rieserferner pluton in the framework of the Oligo-Miocene tectonics of the Eastern Alps. *Journal of Structural Geology*, 116, 64–80. <https://doi.org/10.1016/j.jsg.2018.08.004>
- Dempsey, E., Holdsworth, R., Imber, J., Bistacchi, A., & Di Toro, G. (2014). A geological explanation for intraplate earthquake clustering complexity: The zeolite-bearing fault/fracture networks in the Adamello Massif (Southern Italian Alps). *Journal of Structural Geology*, 66, 58–74. <https://doi.org/10.1016/j.jsg.2014.04.009>
- Diehl, T., Kraft, T., Kissling, E., & Wiemer, S. (2017). The induced earthquake sequence related to the St. Gallen deep geothermal project (Switzerland): Fault reactivation and fluid interactions imaged by microseismicity. *Journal of Geophysical Research: Solid Earth*, 122(9), 7272–7290. <https://doi.org/10.1002/2017jb014473>

- Edwards, B., Kraft, T., Cauzzi, C., Kästli, P., & Wiemer, S. (2015). Seismic monitoring and analysis of deep geothermal projects in St Gallen and Basel, Switzerland. *Geophysical Journal International*, 201(2), 1022–1039. <https://doi.org/10.1093/gji/ggv059>
- Ellsworth, W. L. (2013). Injection-induced earthquakes. *Science*, 341(6142), 1225942. <https://doi.org/10.1126/science.1225942>
- Ellsworth, W. L., Giardini, D., Townend, J., Ge, S., & Shimamoto, T. (2019). Triggering of the Pohang, Korea, earthquake (Mw 5.5) by enhanced geothermal system stimulation. *Seismological Research Letters*, 90(5), 1844–1858. <https://doi.org/10.1785/0220190102>
- Evans, K. F., Genter, A., & Sausse, J. (2005). Permeability creation and damage due to massive fluid injections into granite at 3.5 km at Soultz: 1. Borehole observations. *Journal of Geophysical Research*, 110(B4), B04203. <https://doi.org/10.1029/2004jb003168>
- Evans, K. F., Moriya, H., Niitsuma, H., Jones, R. H., Phillips, W. S., Genter, A., et al. (2005). Microseismicity and permeability enhancement of hydrogeologic structures during massive fluid injections into granite at 3 km depth at the Soultz HDR site. *Geophysical Journal International*, 160(1), 388–412. <https://doi.org/10.1111/j.1365-246x.2004.02474.x>
- Fritsch, K. (1873). Das Gotthardgebiet (mit Karte 1:50000). *Beiträge zur Geologischen Karte der Schweiz*, 15, 164.
- Fu, P., Schoenball, M., Ajo-Franklin, J. B., Chai, C., Maceira, M., Morris, J. P., et al. (2021). Close observation of hydraulic fracturing at EGS Collab Experiment 1: Fracture trajectory, microseismic interpretations, and the role of natural fractures. *Journal of Geophysical Research: Solid Earth*, 126(7), e2020JB020840. <https://doi.org/10.1029/2020JB020840>
- Gholizadeh Doonechaly, N., Bröker, K., Hertrich, M., Ma, X., Obermann, A., Rosskopf, M., et al. (2024). Exploring dominant flow path effects on seismic propagation patterns: A case study of BULGG. *International Journal of Geomechanics*. under preparations.
- Gholizadeh Doonechaly, N., Bröker, K., Hertrich, M., Rosskopf, M., Obermann, A., Durand, V., et al. (2024). Insights from subsurface monitoring for engineering of the stimulation pattern in fractured reservoirs. *Rock Mechanics and Rock Engineering*.
- Gholizadeh Doonechaly, N., Bröker, K., Ma, X., Scarabello, L., Villiger, L., Wenning, Q., et al. (2023). Flow path alterations during hydraulic stimulation at Bedretto underground laboratory for geosciences and geoenergies. *Geothermal Resources Council—Transactions*, 47, 2746–2759.
- Gholizadeh Doonechaly, N., Reinicke, A., Hertrich, M., Plenkers, K., Obermann, A., Fischli, F., et al. (2024). Multiphysics monitoring of cementation operation: Implications for wellbore integrity and hydrogeological characterization. *Environmental Earth Sciences*, 83(5), 146. accepted for publication. <https://doi.org/10.1007/s12665-024-11451-2>
- Giardini, D., Wiemer, S., Maurer, H., Hertrich, M., Meier, P., Alcolea, A., et al. (2022). *Validation of technologies for reservoir engineering (VALTER). Report*. ETH Research Collection. <https://doi.org/10.3929/ethz-b-000644092>
- Gibowicz, S. J., & Kijko, A. (1994). *An introduction to mining seismology* (pp. 265–294). Academic Press.
- Gischig, V., Amann, F., Bethmann, F., Brixel, B., Doetsch, J., Gholizadeh Doonechaly, N., et al. (2020). Hydraulic stimulation and fluid circulation experiments in underground laboratories: Stepping up the scale towards engineered geothermal systems. *Geomechanics for Energy and the Environment*, 24, 100175. <https://doi.org/10.1016/j.gete.2019.100175>
- Gischig, V., Bethmann, F., Hertrich, M., Wiemer, S., Mignan, A., Broccardo, M., et al. (2019). *Induced seismic hazard and risk analysis of hydraulic stimulation experiments at the Bedretto Underground Laboratory for Geosciences and Geoenergies (BULGG)*. ETH Zurich. <https://doi.org/10.3929/ethz-b-000384348>
- Goodman, R. E. (1989). *Introduction to rock mechanics* (p. 562). Wiley.
- Grigoli, F., Cesca, S., Priolo, E., Rinaldi, A. P., Clinton, J. F., Stabile, T. A., et al. (2017). Current challenges in monitoring, discrimination, and management of induced seismicity related to underground industrial activities: A European perspective. *Reviews of Geophysics*, 55(2), 310–340. <https://doi.org/10.1002/2016RG000542>
- Hanks, T. C., & Kanamori, H. (1979). A moment magnitude scale. *Journal of Geophysical Research*, 84(B5), 2348–2350. <https://doi.org/10.1029/jb084ib05p02348>
- Häring, M. O., Schanz, U., Ladner, F., & Dyer, B. C. (2008). Characterisation of the Basel 1 enhanced geothermal system. *Geothermics*, 37(5), 469–495. <https://doi.org/10.1016/j.geothermics.2008.06.002>
- Hillers, G., Husen, S., Obermann, A., Planes, T., Larose, E., & Campillo, M. (2015). Noise-based monitoring and imaging of aseismic transient deformation induced by the 2006 Basel reservoir stimulation. *Geophysics*, 80(4), KS51–KS68. <https://doi.org/10.1190/geo2014-0455.1>
- Hirschberg, S., Wiemer, S., & Burgherr, P. (2015). Energy from the Earth: Deep geothermal as a resource for the future? *TA-Swiss*, 62. <https://doi.org/10.3218/3655-8>
- Horálek, J., Jechumtálková, Z., Dorbath, L., & Šílený, J. (2010). Source mechanisms of micro-earthquakes induced in a fluid injection experiment at the HDR site Soultz-sous-Forêts (Alsace) in 2003 and their temporal and spatial variations. *Geophysical Journal International*, 181, 1547–1565. <https://doi.org/10.1111/j.1365-246x.2010.04506.x>
- Jaeger, J. C., Cook, N. G. W., & Zimmerman, R. (2007). Fundamentals of rock mechanics, Wiley, fundamentals of rock mechanics (4th ed., p. 488).
- Jalali, M., Gischig, V., Doetsch, J., Näf, R., Krietsch, H., Klepikova, M., et al. (2018). Transmissivity changes and microseismicity induced by small-scale hydraulic fracturing tests in crystalline rock. *Geophysical Research Letters*, 45(5), 2265–2273. <https://doi.org/10.1002/2017gl076781>
- Kneafsey, T. J., Dobson, P., Blankenship, D., Morris, J., Knox, H., Schwering, P., et al. (2018). An overview of the EGS collab project: Field validation of coupled process modeling of fracturing and fluid flow at the Sanford underground research facility, Lead, SD. In *43rd workshop on geothermal reservoir engineering* (Vol. 2018).
- Kraft, T., & Deichmann, N. (2014). High-precision relocation and focal mechanism of the injection-induced seismicity at the Basel EGS. *Geothermics*, 52, 59–73. <https://doi.org/10.1016/j.geothermics.2014.05.014>
- Krietsch, H., Gischig, V. S., Doetsch, J., Evans, K. F., Villiger, L., Jalali, M., et al. (2020). Hydromechanical processes and their influence on the stimulation effected volume: Observations from a decameter-scale hydraulic stimulation project. *Solid Earth*, 11(5), 1699–1729. <https://doi.org/10.5194/se-11-1699-2020>
- Krischer, L., Smith, J., Lei, W., Lefebvre, M., Ruan, Y., de Andrade, E. S., et al. (2016). An adaptable seismic data format. *Geophysical Supplements to the Monthly Notices of the Royal Astronomical Society*, 207(2), 1003–1011. <https://doi.org/10.1093/gji/ggw319>
- Kwiatek, G., & Ben-Zion, Y. (2013). Assessment of P and S wave energy radiated from very small shear-tensile seismic events in a deep South African mine. *Journal of Geophysical Research: Solid Earth*, 118(7), 3630–3641. <https://doi.org/10.1002/jgrb.50274>
- Kwiatek, G., Martínez-Garzón, P., Plenkers, K., Leonhardt, M., Zang, A., von Specht, S., et al. (2018). Insights into complex subdecimeter fracturing processes occurring during a water injection experiment at depth in Äspö Hard Rock Laboratory, Sweden. *Journal of Geophysical Research: Solid Earth*, 123(8), 6616–6635. <https://doi.org/10.1029/2017jb014715>
- Kwiatek, G., Plenkers, K., & Dresen, G., & JAGUARS Research Group. (2011). Source parameters of picoseismicity recorded at Mponeng deep gold mine, South Africa: Implications for scaling relations. *Bulletin of the Seismological Society of America*, 101(6), 2592–2608. <https://doi.org/10.1785/0120110094>

- Kwiatek, G., Saarno, T., Ader, T., Bluemle, F., Bohnhoff, M., Chendorain, M., et al. (2019). Controlling fluid-induced seismicity during a 6.1-km-deep geothermal stimulation in Finland. *Science Advances*, 5(5), eaav7224. <https://doi.org/10.1126/sciadv.aav7224>
- Leonard, M., & Kennett, B. L. N. (1999). Multi-component autoregressive techniques for the analysis of seismograms. *Physics of the Earth and Planetary Interiors*, 113(1–4), 247–263. [https://doi.org/10.1016/s0031-9201\(99\)00054-0](https://doi.org/10.1016/s0031-9201(99)00054-0)
- Lützenkirchen, V., & Loew, S. (2011). Late Alpine brittle faulting in the Rotondo granite (Switzerland): Deformation mechanisms and fault evolution. *Swiss Journal of Geosciences*, 104(1), 31–54. <https://doi.org/10.1007/s0015-010-0050-0>
- Ma, X., Hertrich, M., Amann, F., Bröker, K., Ghazizadeh Doonechaly, N., Gischig, V., et al. (2022). Multi-disciplinary characterizations of the BedrettoLab—A new underground geoscience research facility. *Solid Earth*, 13(2), 301–322. <https://doi.org/10.5194/se-13-301-2022>
- Madariaga, R. (1976). Dynamics of an expanding circular fault. *Bulletin of the Seismological Society of America*, 66(3), 639–666. <https://doi.org/10.1785/ssa0660030639>
- Maeda, N. (1985). A method for reading and checking phase times in autoprocessing system of seismic wave data. In *Zisin* (Vol. 38, pp. 365–379). https://doi.org/10.4294/zisin1948.38.3_36
- Manthei, G., Eisenblätter, J., & Dahn, T. (2001). Moment tensor evaluation of acoustic emission sources in salt rock. *Construction and Building Materials*, 15(5–6), 297–309. [https://doi.org/10.1016/s0950-0618\(00\)00078-7](https://doi.org/10.1016/s0950-0618(00)00078-7)
- Manthei, G., & Plenkers, K. (2018). Review on in situ acoustic emission monitoring in the context of structural health monitoring in mines. *Applied Sciences*, 8(9), 1595. <https://doi.org/10.3390/app8091595>
- McGarr, A. (1971). Violent deformation of rock near deep-level tabular excavations—Seismic events. *Bulletin of the Seismological Society of America*, 61, 1453–1466.
- McGarr, A. (2014). Maximum magnitude earthquakes induced by fluid injection. *Journal of Geophysical Research: Solid Earth*, 119(2), 1008–1019. <https://doi.org/10.1002/2013jb010597>
- Meier, P., & Christe, F. (2023). *Zonal isolation, drilling and exploitation of EGS projects, final report of project ZoDrEx to Swiss Federal Office of Energy, GeoEnergie Suisse*. Bern. Retrieved from <https://www.aramis.admin.ch/Default?DocumentID=70241&Load=true>
- Meier, P., Guinot, F., Bethmann, F., Faschingbauer, R., Alcolea, A., Liautaud, F., et al. (2020). ZoDrEx an European endeavour for optimising zonal isolation, drilling and exploitation of EGS projects. In *Proceedings world geothermal congress* (p. 1).
- Meier, P. M., Rodríguez, A. A., & Bethmann, F. (2015). Lessons learned from Basel: New EGS projects in Switzerland using multistage stimulation and a probabilistic traffic light system for the reduction of seismic risk. In *Proceedings of world geothermal congress* (pp. 19–25).
- Mignan, A., Broccardo, B., Wiemer, S., & Giardini, D. (2017). Induced seismicity closed-form traffic light system for actuarial decision-making during deep fluid injections. *Scientific Reports*, 7(1), 13607. <https://doi.org/10.1038/s41598-017-13585-9>
- Mukuhira, Y., Dinske, C., Asanuma, H., Ito, T., & Häring, M. O. (2017). Pore pressure behavior at the shut-in phase and causality of large induced seismicity at Basile, Switzerland. *Journal of Geophysical Research: Solid Earth*, 122(1), 411–435. <https://doi.org/10.1002/2016jb013338>
- Naoi, M., Nakatani, M., Igarashi, T., Otsuki, K., Yabe, Y., Kgarume, T., et al. (2015). Unexpectedly frequent occurrence of very small repeating earthquakes ($-5.1 \leq M_w \leq -3.6$) in a South African gold mine: Implications for monitoring intraplate faults. *Journal of Geophysical Research: Solid Earth*, 120(12), 8478–8493. <https://doi.org/10.1002/2015jb012447>
- Naoi, M., Nakatani, M., Kgarume, T., Khambule, S., Masakale, T., Ribeiro, L., et al. (2015). Quasi-static slip patch growth to 20 m on a geological fault inferred from acoustic emissions in a South African gold mine. *Journal of Geophysical Research: Solid Earth*, 120(3), 1692–1707. <https://doi.org/10.1002/2014jb011165>
- Naoi, M., Nakatani, M., Otsuki, K., Yabe, Y., Kgarume, T., Murakami, O., et al. (2015). Steady activity of microfractures on geological faults loaded by mining stress. *Tectonophysics*, 649, 100–114. <https://doi.org/10.1016/j.tecto.2015.02.025>
- Naoi, M., Nakatani, M., Yabe, Y., Kwiatek, G., Igarashi, T., & Plenkers, K. (2011). Twenty thousand aftershocks of a very small (M2) earthquake and their relation to the mainshock rupture and geological structures. *Bulletin of the Seismological Society of America*, 101(5), 2399–2407. <https://doi.org/10.1785/0120100346>
- Norbeck, J. H., & Latimer, T. (2023). Commercial-scale demonstration of a first-of-a-kind enhanced geothermal system. *EartharXiv*. <https://doi.org/10.31223/X52X0B>
- Obermann, A., Kraft, T., Larose, E., & Wiemer, S. (2015). Potential of ambient seismic noise techniques to monitor the St. Gallen geothermal site (Switzerland). *Journal of Geophysical Research: Solid Earth*, 120(6), 4301–4316. <https://doi.org/10.1002/2014jb011817>
- Pagani, M., Monelli, D., Weatherill, G., Danciu, L., Crowley, H., Silva, V., et al. (2014). OpenQuake engine: An open hazard (and risk) software for the global earthquake model. *Seismological Research Letters*, 85(3), 692–702. <https://doi.org/10.1785/0220130087>
- Papadopoulos, I. S., & Cooper, H. H., Jr. (1967). Drawdown in a well of large diameter. *Water Resources Research*, 3(1), 241–244. <https://doi.org/10.1029/wr003i001p00241>
- Plenkers, K. (2010). On the characteristics of mining-induced seismicity with magnitudes $-5 < M_w < -1$. 2010. Ph.D. Thesis.
- Plenkers, K., Manthei, G., & Kwiatek, G. (2022). Underground in-situ acoustic emission study of rock stability and earthquake physics, acoustic emission testing. In C. U. Grosse, et al. (Eds.). *Springer tracts in civil engineering*. https://doi.org/10.1007/978-3-030-67936-1_16
- Plenkers, K., Reinicke, A., Obermann, A., Ghazizadeh Doonechaly, N., Krietsch, H., Fechner, T., et al. (2023). Multi-disciplinary monitoring networks for mesoscale underground experiments: Advances in the Bedretto reservoir project. *Sensors*, 23(6), 3315. <https://doi.org/10.3390/s23063315>
- Poita, N., Satriano, C., Villette, J. P., Bernard, P., & Obara, K. (2016). Multiband array detection and location of seismic sources recorded by dense seismic networks. *Geophysical Journal International*, 205(3), 1548–1573. <https://doi.org/10.1093/gji/ggw071>
- Rast, M., Galli, A., Ruh, J. B., Guillong, M., & Madonna, C. (2022). Geology along the Bedretto tunnel: Kinematic and geochronological constraints on the evolution of the Gotthard Massif (Central Alps). *Swiss Journal of Geosciences*, 115(1), 8. <https://doi.org/10.1186/s00015-022-00409-w>
- Renard, P. (2017). Hytool: An open source matlab toolbox for the interpretation of hydraulic tests using analytical solutions. *Journal of Open Source Software*, 2(19), 441. <https://doi.org/10.21105/joss.00441>
- Roschkopf, M., Durand, V., & Obermann, A. (2024c). Seismic catalogs for the 2022–2023 hydraulic stimulation experiments at the Bedretto underground laboratory [Dataset]. *ETH Research Collection*. <https://doi.org/10.3929/ethz-b-000658218>
- Roschkopf, M., Durand, V., Plenkers, P., Villiger, L., Giardini, D., & Obermann, A. (2024b). Accuracy of picoseismic catalogs in hectometer-scale in-situ experiments, SRL.
- Roschkopf, M., Durand, V., Villiger, L., Doetsch, J., Obermann, A., & Krischer, L. (2024d). DUGseis processing example with needed data files [Software]. *Zenodo*. <https://doi.org/10.5281/zenodo.10598393>
- Roschkopf, M., Durand, V., Villiger, V., Doetsch, J., Obermann, A., & Krischer, L. (2024a). DUGseis: A Python package for real-time and post-processing of picoseismicity. *Journal of Open Source Software*.

- Rutledge, J. T., Phillips, W. S., & Mayerhofer, M. J. (2004). Faulting induced by forced fluid injection and fluid flow forced by faulting: An interpretation of hydraulic-fracture microseismicity, Carthage Cotton Valley gas field, Texas. *Bulletin of the Seismological Society of America*, 94(5), 1817–1830. <https://doi.org/10.1785/012003257>
- Rutsch, R. F., & Pruvost, P. (1966). Lexique stratigraphique international. I, 653. Europe, fasc. 7c: Alpes suisses et Tessin méridional.
- Sánchez-Pastor, P., Obermann, A., Schimmel, M., Weemstra, C., Verdel, A., & Jousset, P. (2019). Short- and long-term variations in the Reykjanes geothermal reservoir from seismic noise interferometry. *Geophysical Research Letters*, 46(11), 5788–5798. <https://doi.org/10.1029/2019GL082352>
- Sánchez-Pastor, P., Wu, S.-M., Hokstad, K., Kristjánsson, B., Drouin, V., Ducrocq, C., et al. (2023). Monitoring gas pockets in the crust with seismic noise. *Nature Communications and Environment*, 4(1), 453. <https://doi.org/10.1038/s43247-023-01122-8>
- Scarabello, L., & Diehl, T. (2021). swiss-seismological-service/scrtdd [Software]. Zenodo. <https://doi.org/10.5281/zenodo.5337361>
- Schmid, S. M., Pfiffner, O. A., Froitzheim, N., Schönborn, G., & Kissling, G. (1996). Geophysical-geological transect and tectonic evolution of the Swiss-Italian Alps. *Tectonics*, 15(5), 1036–1064. <https://doi.org/10.1029/96TC00433>
- Sergeev, S. A., & Steiger, R. H. (1995). Caledonian and Variscan granitoids of the Gotthard Massif: New geochronological and geochemical results. *Schweizerische Mineralogische und Petrographische Mitteilungen*, 75, 315–316.
- Shapiro, S. A., Dinske, C., & Kummerow, J. (2007). Probability of a given-magnitude earthquake induced by a fluid injection. *Geophysical Research Letters*, 34(22), L22314. <https://doi.org/10.1029/2007GL031615>
- Shapiro, S. A., Dinske, C., Langenbruch, C., & Wenzel, F. (2010). Seismogenic index and magnitude probability of earthquakes induced during reservoir fluid stimulations. *The Leading Edge*, 29(3), 304–309. <https://doi.org/10.1190/1.3353727>
- Steck, A., & Burri, G. (1971). Chemismus und paragenesen von granaten aus granitgneisen der grünschiefer-und amphibolitfazies der zentralalpen. *Schweiz Mineral Petrogr Mitt*, 51, 534–538.
- Taira, T., Nayak, A., Brenguier, F., & Manga, M. (2018). Monitoring reservoir response to earthquakes and fluid extraction, Salton Sea geothermal field, California. *Science Advances*, 4(1), e1701536. <https://doi.org/10.1126/sciadv.1701536>
- Toledo, T., Obermann, A., Verdel, A., Martins, J. E., Jousset, P., Mortensen, A. K., et al. (2022). Ambient seismic noise monitoring and imaging at the Theistareyki geothermal field (Iceland). *Journal of Volcanology and Geothermal Research*, 429, 107590. <https://doi.org/10.1016/j.jvolgeores.2022.107590>
- Van Aswegen, G. (2005). Routine seismic hazard assessment in some South African mines. In Y. Potvin, & M. Hudyma (Eds.), *Rockbursts and seismicity in mines, RaSiM6* (pp. 437–444).
- Van der Elst, N. J., Page, M. T., Weiser, D. A., Goebel, T. H., & Hosseini, S. M. (2016). Induced earthquake magnitudes are as large as (statistically) expected. *Journal of Geophysical Research: Solid Earth*, 121(6), 4575–4590. <https://doi.org/10.1002/2016jb012818>
- Villiger, L., Gischig, V. S., Doetsch, J., Krietsch, H., Dutler, N. O., Jalali, M., et al. (2020). Influence of reservoir geology on seismic response during decameter-scale hydraulic stimulations in crystalline rock. *Solid Earth*, 11(2), 627–655. <https://doi.org/10.5194/se-11-627-2020>
- Villiger, L., Gischig, V. S., Kwiatek, G., Krietsch, H., Doetsch, J., Jalali, M., et al. (2021). Meter-scale stress heterogeneities and stress redistribution drive complex fracture slip and fracture growth during a hydraulic stimulation experiment. *Geophysical Journal International*, 225(3), 1689–1703. <https://doi.org/10.1093/gji/ggab057>
- Waldhauser, F. (2001). HypoDD: A computer program to compute double-difference earthquake locations. *Open-File Report*, 01-113. U.S. Geological Survey.
- Waldhauser, F., & Ellsworth, W. L. (2000). A double-difference earthquake location algorithm: Method and application to the northern Hayward fault, California. *Bulletin of the Seismological Society of America*, 90(6), 1353–1368. <https://doi.org/10.1785/0120000006>
- Wiemer, S. (2000). Introducing probabilistic aftershock hazard mapping. *Geophysical Research Letters*, 27(20), 3405–3408. <https://doi.org/10.1029/2000GL011479>
- Yabe, Y., Nakatani, M., Naoi, M., Philipp, J., Janssen, C., Watanabe, T., et al. (2015). Nucleation process of an M2 earthquake in a deep gold mine in South Africa inferred from on-fault foreshock activity: On-fault foreshocks of M2 earthquake. *Journal of Geophysical Research: Solid Earth*, 120(8), 5574–5594. <https://doi.org/10.1002/2014JB011680>
- Ye, Z., & Ghassemi, A. (2018). Injection-induced shear slip and permeability enhancement in granite fractures. *Journal of Geophysical Research: Solid Earth*, 123(10), 9009–9032. <https://doi.org/10.1029/2018JB016045>
- Yeo, I. W., Brown, M. R. M., Ge, S., & Lee, K. K. (2020). Causal mechanism of injection-induced earthquakes through the M-w 5.5 Pohang earthquake case study. *Nature Communications*, 11(1), 2614. <https://doi.org/10.1038/s41467-020-16408-0>
- Zang, A., Stephansson, O., Stenberg, L., Plenkers, K., Specht, S., Milkereit, C., et al. (2017). Hydraulic fracture monitoring in hard rock at 410 m depth with an advanced fluid-injection protocol and extensive sensor array. *Geophysical Journal International*, 208(2), 790–813. <https://doi.org/10.1093/gji/ggw430>
- Zang, A., Stephansson, O., & Zimmermann, G. (2020). Impact of injection style on the evolution of fluid-induced seismicity and permeability in rock mass at 410 m depth in Äspö hard rock laboratory, Sweden. In B. Shen, O. Stephansson, & M. Rinne (Eds.), *Modelling rock fracturing processes*. Springer. https://doi.org/10.1007/978-3-030-35525-8_5
- Zhang, S., Ma, X., Bröker, K., van Limborgh, R., Wenning, Q., Hertrich, M., & Giardini, D. (2023). Fault zone spatial stress variations in a granitic rock mass: Revealed by breakouts within an array of boreholes. *Journal of Geophysical Research: Solid Earth*, 128(8), e2023JB026477. <https://doi.org/10.1029/2023JB026477>